




## Compatibility relationships in van der Waals quasicrystals

Guodong Yu <sup>1,2</sup>, Yunhua Wang,<sup>2,3,4,\*</sup> Mikhail I. Katsnelson <sup>4</sup>, Hai-Qing Lin,<sup>3,5</sup> and Shengjun Yuan <sup>2,3,4,†</sup>

<sup>1</sup>Center for Quantum Sciences and School of Physics, Northeast Normal University, Changchun 130024, China

<sup>2</sup>Key Laboratory of Artificial Micro- and Nano-structures of Ministry of Education and School of Physics and Technology, Wuhan University, Wuhan 430072, China

<sup>3</sup>Beijing Computational Science Research Center, Beijing, 100193, China

<sup>4</sup>Institute for Molecules and Materials, Radboud University, Heijendaalseweg 135, NL-6525 AJ Nijmegen, Netherlands

<sup>5</sup>School of Physics, Zhejiang University, Hangzhou, 310027, China



(Received 7 March 2022; accepted 2 August 2022; published 9 August 2022)

The incommensurate twist structure and the interlayer coupling induce van der Waals quasicrystals (vdW-QCs). Replacing conventional band theory requiring translational symmetry, the resonant coupling Hamiltonian endowing the quasiband structure in  $\mathbf{k}$  space is adopted to describe electronic properties of vdW-QCs [Moon *et al.*, *Phys. Rev. B* **99**, 165430 (2019)]. Here we investigate the symmetries of the resonant coupling Hamiltonians in dodecagonal and octagonal vdW-QCs. Through symmetry analyses we derive compatibility relationships (CRs) between  $\Gamma$  point and other irreducible pathways and predict the symmetry changes and band splits. Especially, we find that from  $\Gamma$  point to Brillouin zone corner points of monolayers, arbitrary twofold degenerate states are split into one  $A'$  and one  $A''$  state, and from  $\Gamma$  point to the intersection points of two Brillouin zones of monolayers, arbitrary twofold degenerate states are split into one  $A$  and one  $B$  state. Instead of projection operation analyses, we discuss the CRs of different point groups between the coupled bilayers and uncoupled monolayers to construct the interlayer hybridization selection rules (IHSRs) [Yu *et al.*, *Phys. Rev. B* **105**, 125403 (2022)], which govern how the interlayer states interact with each other in the resonant coupling systems of dodecagonal and octagonal vdW-QCs. These derived IHSRs indicate that the first two main resonant couplings allow the nonequivalent hybridizations only between  $B_1$  and  $B_2$  states and the equivalent hybridizations for  $A$ ,  $A_i$ ,  $A'$ ,  $A''$ ,  $E$ , or  $E_i$  states.

DOI: [10.1103/PhysRevB.106.075121](https://doi.org/10.1103/PhysRevB.106.075121)

### I. INTRODUCTION

A van der Waals quasicrystal (vdW-QC) of bilayer lattices emerges when two copies of a periodic pattern are overlaid with a high-symmetrical incommensurate twist, such as  $30^\circ$ -twisted bilayer hexagon lattices (dodecagonal vdW-QC) with 12-fold symmetry and  $45^\circ$ -twisted bilayer square lattices (octagonal vdW-QC) with eightfold symmetry. The dodecagonal bilayer graphene vdW-QC (i.e., graphene quasicrystal) has been fabricated experimentally on top of various metal surfaces [1–9]. Many peculiar physical properties make graphene quasicrystal quite distinctive from graphene monolayer, such as multiple Dirac cones with 12-fold rotational symmetry [1], the sensitive dependence on an electric field and a pressure [10,11], unbalanced electron distributions [4], quantum oscillations with spiral Fermi surfaces [12], and fractal features for a low friction [13].

Compared with conventional quasicrystals, in which all of the sites are intrinsically located within the quasiperiodic order [14,15], a vdW-QC can be viewed as the extrinsic quasicrystal because its quasiperiodicity originates from the interlayer coupling and the high-symmetrical incommensu-

rate twist structure. Due to the absence of the periodicity, the conventional band theory for periodical crystallines is not suitable for vdW-QCs. Alternatively, the resonant coupling Hamiltonians capture the electronic structures and properties of vdW-QCs by virtue of the quasiband structure [11,16], which refers to the energy  $\mathbb{E}(\mathbf{k}_0)$  of the resonant coupling Hamiltonian as a function of the wave vector  $\mathbf{k}_0$  with  $\mathbf{k}_0$  within the set of  $\mathbf{k}$  points inside the first Brillouin zone (BZ) of monolayer. In periodical crystallines, compatibility relationships (CRs) of the band structure, i.e., the relationships between irreducible representations at different  $\mathbf{k}$  points, are of importance for characterizing symmetry changes and band splits. However, the CRs of quasiband structures for vdW-QCs are not discussed in literature up to date. On the other hand, the interlayer coupling is responsible for the origin and peculiar physical properties of an extrinsic quasicrystal. Recently, the interlayer hybridization selection rules (IHSRs) [17] have been established to describe how the states from two layers couple with each other within the real-space symmetries in bilayer graphene systems. However, the IHSRs for the resonant couplings of vdW-QCs in  $\mathbf{k}$  space are still not discussed.

Herein, we systematically investigate the symmetries of both the first and second strongest resonant coupling Hamiltonians in dodecagonal and octagonal vdW-QCs. Our symmetry analyses show that (i) the Hamiltonian has the highest  $\mathbb{D}_{nd}$  symmetries at  $\Gamma$  point for the first ( $n = 6$ ) and second ( $n = 2$ )

\*wangyunhua@csrc.ac.cn

†s.yuan@whu.edu.cn

strongest resonant couplings in dodecagonal vdW-QC and for both first two strongest resonant couplings in octagonal vdW-QC with  $n = 4$ , and (ii) the Hamiltonian has respectively  $\mathbb{C}_s$  and  $\mathbb{C}_2$  symmetries for the irreducible pathway of  $-\mathbf{k}_x$  and the irreducible pathway from  $\Gamma$  point to the intersection points of two Brillouin zones of monolayers. Through these symmetry analyses we derive the CRs of quasiband structures and predict the symmetry changes and band splits along these irreducible pathways. Instead of previous projection operation analyses determining the IHSRs, we alternatively discuss the CRs of different point groups between the coupled bilayers and uncoupled monolayers to derive the IHSRs of both the first two strongest resonant couplings in dodecagonal and octagonal vdW-QCs. Our further numerical calculations of the energy spectra and nonzero interlayer hybridization matrix element distributions identify these IHSRs predicted by the CRs.

The paper is organized as follows. In Sec. II we present the structures and symmetries of dodecagonal and octagonal vdW-QCs. In Sec. III we describe the model and construct the resonant coupling Hamiltonians. In Sec. IV we discuss the symmetries of the Hamiltonians of the first two strongest resonant couplings in the two vdW-QCs. In Sec. V we derive the CRs of quasiband structures and discuss symmetry changes and band splits. In Sec. VI we discuss the IHSRs for both the first two strongest resonant couplings and perform numerical verifications. In Sec. VII we discuss the strategy to realize the octagonal vdW-QC. Finally, we conclude our results and findings in Sec. VIII.

## II. STRUCTURES AND SYMMETRIES

The structure of a vdW-QC is determined by its lattice vectors of two component layers ( $\mathbf{a}_1^b, \mathbf{a}_2^b$ ) and ( $\mathbf{a}_1^t, \mathbf{a}_2^t$ ), relative positions of all sublattices inside one unit cell ( $\boldsymbol{\tau}_X^b$  and  $\boldsymbol{\tau}_X^t$ ) with the sublattice index  $X$ , and the interlayer distance  $h$ . Superscripts  $b$  and  $t$  denote the bottom and top layers, respectively. Positions of all sites in  $xy$  plane are determined by

$$\begin{aligned} \mathbf{R}_X^b &= m\mathbf{a}_1^b + n\mathbf{a}_2^b + \boldsymbol{\tau}_X^b, \\ \mathbf{R}_X^t &= m\mathbf{a}_1^t + n\mathbf{a}_2^t + \boldsymbol{\tau}_X^t, \end{aligned} \quad (1)$$

where  $m$  and  $n$  run over all integer values.

Dodecagonal vdW-QCs are  $30^\circ$  twisted bilayer hexagon lattices. The lattice vectors are  $\mathbf{a}_1^b = a(\frac{\sqrt{3}}{2}, -\frac{1}{2})$ ,  $\mathbf{a}_2^b = a(\frac{\sqrt{3}}{2}, \frac{1}{2})$ ,  $\mathbf{a}_1^t = R(\frac{\pi}{6})\mathbf{a}_1^b = a(1, 0)$ , and  $\mathbf{a}_2^t = R(\frac{\pi}{6})\mathbf{a}_2^b = a(\frac{1}{2}, \frac{\sqrt{3}}{2})$ , where  $R(\theta)$  is the rotation operation around the  $z$  axis by  $\theta$  anticlockwise. The reciprocal lattice vectors of the two layers are  $\mathbf{b}_1^b = \frac{2\pi}{a}(\frac{1}{\sqrt{3}}, -1)$ ,  $\mathbf{b}_2^b = \frac{2\pi}{a}(\frac{1}{\sqrt{3}}, 1)$ ,  $\mathbf{b}_1^t = \frac{2\pi}{a}(1, -\frac{1}{\sqrt{3}})$ , and  $\mathbf{b}_2^t = \frac{2\pi}{a}(0, \frac{2}{\sqrt{3}})$ . The relative positions of sublattices  $A$  and  $B$  are  $\boldsymbol{\tau}_A^b = \frac{1}{3}\mathbf{a}_1^b + \frac{1}{3}\mathbf{a}_2^b$ ,  $\boldsymbol{\tau}_B^b = \frac{2}{3}\mathbf{a}_1^b + \frac{2}{3}\mathbf{a}_2^b$ ,  $\boldsymbol{\tau}_A^t = \frac{1}{3}\mathbf{a}_1^t + \frac{1}{3}\mathbf{a}_2^t$ , and  $\boldsymbol{\tau}_B^t = \frac{2}{3}\mathbf{a}_1^t + \frac{2}{3}\mathbf{a}_2^t$ .

Octagonal vdW-QCs are  $45^\circ$ -twisted bilayer square lattices. The lattice vectors are  $\mathbf{a}_1^b = a(\frac{\sqrt{2}}{2}, -\frac{\sqrt{2}}{2})$ ,  $\mathbf{a}_2^b = a(\frac{\sqrt{2}}{2}, \frac{\sqrt{2}}{2})$ ,  $\mathbf{a}_1^t = R(\frac{\pi}{4})\mathbf{a}_1^b = a(1, 0)$ , and  $\mathbf{a}_2^t = R(\frac{\pi}{4})\mathbf{a}_2^b = a(0, 1)$ . The reciprocal lattice vectors are  $\mathbf{b}_1^b = \frac{2\pi}{a}(\frac{\sqrt{2}}{2}, -\frac{\sqrt{2}}{2})$ ,  $\mathbf{b}_2^b = \frac{2\pi}{a}(\frac{\sqrt{2}}{2}, \frac{\sqrt{2}}{2})$ ,  $\mathbf{b}_1^t = \frac{2\pi}{a}(1, 0)$ , and  $\mathbf{b}_2^t = \frac{2\pi}{a}(0, 1)$ . There is

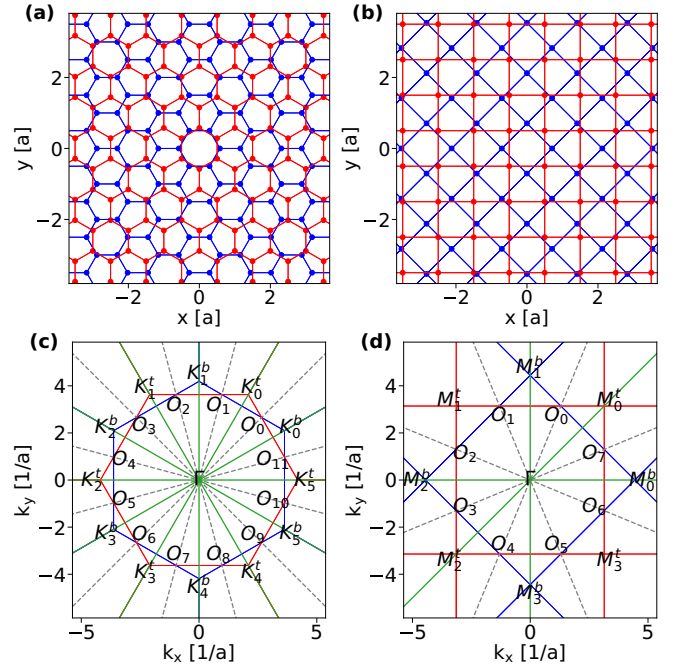


FIG. 1. Top views of lattice structures for  $\mathbb{D}_{6d}$  dodecagonal vdW-QC in (a) and  $\mathbb{D}_{4d}$  octagonal vdW-QC in (b). Their corresponding BZs for two component layers in (c) and (d). The green solid and gray dashed lines in (c) and (d) stand for the reflection mirrors and the axes of twofold rotations in reciprocal spaces, respectively.

only one sublattice in square lattices, and its relative positions are  $\boldsymbol{\tau}^b = \frac{1}{2}\mathbf{a}_1^b + \frac{1}{2}\mathbf{a}_2^b$  and  $\boldsymbol{\tau}^t = \frac{1}{2}\mathbf{a}_1^t + \frac{1}{2}\mathbf{a}_2^t$ .

The octagonal vdW-QC has  $\mathbb{D}_{6d}$  symmetries for its structure and BZs in Figs. 1(a) and 1(c), and the octagonal vdW-QC has  $\mathbb{D}_{4d}$  symmetries for its structure and BZs in Figs. 1(b) and 1(d). We next only discuss symmetries in reciprocal space because the resonant coupling Hamiltonian (see Secs. III B and IV) describing the quasicrystalline resonant states is based on the  $\mathbf{k}$ -space tight-binding model.  $\mathbb{D}_{nd}$  ( $n = 6$  and  $4$ ) point groups consist of rotation operations  $C_n^i$  with the identity operation  $E$ , improper rotation operations  $S_{2n}^{2i+1}$ , twofold rotation operations  $C_{2,i}^t$ , and reflections  $\sigma_{d,i}$  with  $i = 0, 1, \dots, n-1$ . For their BZs shown in Figs. 1(c) and 1(d), these symmetry operations read

$$\begin{aligned} C_n^i &= R\left(\frac{2\pi}{n}i\right), \\ S_{2n}^{2i+1} &= \sigma_h R\left(\frac{2\pi}{n}i + \frac{\pi}{n}\right), \\ \sigma_{d,i} &= R\left(\frac{2\pi}{n}i\right)\sigma_{d,0}\left[R\left(\frac{2\pi}{n}i\right)\right]^\dagger, \\ C_{2,i}^t &= \sigma_h R\left(\frac{\pi}{n}i + \frac{\pi}{2n}\right)\sigma_{d,0}\left[R\left(\frac{\pi}{n}i + \frac{\pi}{2n}\right)\right]^\dagger, \end{aligned} \quad (2)$$

where  $\sigma_h$  is the reflection with the  $xy$  mirror plane,  $\sigma_{d,0} = \sigma_x$  is chosen in this paper, and the rotation axis of  $C_{2,i}^t$  bisects the mirrors of  $\sigma_{d,i}$  and  $\sigma_{d,i+1}$ . Besides, we have  $\sigma_{d,\frac{n}{2}} = \sigma_y$  with  $yz$  plane being the mirror.

The BZs of two component layers for the  $\mathbb{D}_{6d}$  dodecagonal BZ are  $\mathbb{C}_{6v}$  symmetrical, and the BZs of two component

layers for the  $\mathbb{D}_{4d}$  octagonal BZ are  $\mathbb{C}_{4v}$  symmetrical. Therefore, the interlayer couplings described in the  $\mathbf{k}$  space have the symmetry restriction  $\mathbb{C}_{nv} + \mathbb{C}_{nv} \Rightarrow \mathbb{D}_{nd}$ , where  $n = 6$  and  $n = 4$  are for dodecagonal and octagonal vdW-QCs, respectively. The point group  $\mathbb{C}_{nv}^{b/t}$  includes the rotations  $C_n^i$  with  $i = 0, 1, \dots, n-1$  and two classes of reflections  $\sigma_{v,i}^{b/t}$  and  $\sigma_{d,i}^{b/t}$  with  $i = 0, 1, \dots, n/2-1$ . We use the same labels  $C_n^i$  to stand for the rotations around the  $z$  axis because both  $\mathbb{C}_{nv}^b$  and  $\mathbb{C}_{nv}^t$  are the subgroups of  $\mathbb{D}_{nd}$  and the three groups share the same rotations, namely  $C_n^i = R(\frac{2\pi}{n}i)$ . The twist leads to

$$\begin{aligned}\sigma_{v,i}^t &= \sigma_{d,i}^b = R\left(\frac{2\pi}{n}i + \frac{\pi}{6}\right)\sigma_{v,0}^b \left[ R\left(\frac{2\pi}{n}i + \frac{\pi}{6}\right) \right]^\dagger, \\ \sigma_{d,i}^t &= \sigma_{v,j}^b = R\left(\frac{2\pi}{n}j\right)\sigma_{v,0}^b \left[ R\left(\frac{2\pi}{n}j\right) \right]^\dagger,\end{aligned}\quad (3)$$

where  $j = (i+1) \bmod (n/2)$  and  $\sigma_{v,0}^b = \sigma_x$ , which is identical to the  $\sigma_{d,0}$  in  $\mathbb{D}_{nd}$  point group. Therefore, from Eqs. (2) and (3) we note that  $\mathbb{C}_{nv}^b \neq \mathbb{C}_{nv}^t$  due to the twist although both of them have the point group symmetry  $\mathbb{C}_{nv}$ . Equations (2) and (3) are also suitable for the symmetry restriction  $\mathbb{C}_{2v} + \mathbb{C}_{2v} \Rightarrow \mathbb{D}_{2d}$ , which exists in the second strongest resonant coupling (see Sec. III B) in the dodecagonal vdW-QC. We remind readers that, for different symmetry restrictions under consideration, including  $\mathbb{C}_{nv} + \mathbb{C}_{nv} \Rightarrow \mathbb{D}_{nd}$  with  $n = 2, 4, 6$ , the labels  $\sigma_{d,i}$ ,  $\sigma_{v,i}^t$ ,  $\sigma_{v,i}^b$ ,  $\sigma_{d,i}^t$ , and  $\sigma_{d,i}^b$  correspond to different operations, and here we always choose  $\sigma_{d,0}$  in  $\mathbb{D}_{nd}$  and  $\sigma_{v,0}^b$  in  $\mathbb{C}_{nv}^b$  being  $\sigma_x$  as the reflection with the  $xz$  mirror plane.

### III. MODEL AND METHODS

#### A. Tight-binding model

Assuming only one  $p_z$  orbital on each sublattice for both vdW-QCs, the Hamiltonian is described by the two-center Slater-Koster tight-binding model. The hopping energy between sites  $i$  and  $j$  is determined by [18]

$$t(\mathbf{r}_{ij}) = n^2 V_{pp\sigma}(|\mathbf{r}_{ij}|) + (1 - n^2) V_{pp\pi}(|\mathbf{r}_{ij}|), \quad (4)$$

where  $n$  is the direction cosine of relative position vectors  $\mathbf{r}_{ij}$  with respect to the  $z$  axis. The Slater-Koster parameters  $V_{pp\sigma}$  and  $V_{pp\pi}$  read

$$\begin{aligned}V_{pp\pi}(|\mathbf{r}_{ij}|) &= -\gamma_0 e^{(a/\sqrt{3}-|\mathbf{r}_{ij}|)/\delta}, \\ V_{pp\sigma}(|\mathbf{r}_{ij}|) &= \gamma_1 e^{(1.36a-|\mathbf{r}_{ij}|)/\delta}\end{aligned}\quad (5)$$

for dodecagonal vdW-QCs, and

$$\begin{aligned}V_{pp\pi}(|\mathbf{r}_{ij}|) &= -\beta_0 e^{(a-|\mathbf{r}_{ij}|)/\delta}, \\ V_{pp\sigma}(|\mathbf{r}_{ij}|) &= \beta_1 e^{(3a-|\mathbf{r}_{ij}|)/\delta}\end{aligned}\quad (6)$$

for octagonal vdW-QCs. The interlayer distances are  $1.36a$  and  $3a$  for dodecagonal and octagonal vdW-QCs, respectively, and  $\delta = 0.184a$  measures the decay length of the hopping energy with the site-site distance. The octagonal vdW-QCs has not been fabricated experimentally, and for clarity we use similar expressions in Eq. (6) for a twisted bilayer square lattice like that of twisted bilayer graphene. The energy parameters  $\beta_0$  and  $\beta_1$  for real materials with a twisted bilayer square lattice are not necessarily the same as  $\gamma_0$  and  $\gamma_1$  of twisted

bilayer graphene in Eq. (5). For example, using cold atoms in optical lattices to simulate the twisted bilayer square lattice,  $\beta_0$  and  $\beta_1$  can be tuned in a wide range [19–22], as discussed later in Sec. VII. Here we choose  $\beta_0 = \gamma_0$  and  $\beta_1 = \gamma_1$  with  $\gamma_1 = 0.142\gamma_0$ , so that we can have a more direct comparison between two different vdW-QCs.

#### B. Hamiltonian construction for quasicrystalline resonant states

The Bloch bases of two component layers are defined as

$$\begin{aligned}|\mathbf{k}^b, X\rangle &= \frac{1}{\sqrt{N}} \sum_{\mathbf{L}^b} e^{i\mathbf{k}^b \cdot (\mathbf{L}^b + \boldsymbol{\tau}_X^b)} |\mathbf{L}^b + \boldsymbol{\tau}_X^b\rangle, \\ |\mathbf{k}^t, X\rangle &= \frac{1}{\sqrt{N}} \sum_{\mathbf{L}^t} e^{i\mathbf{k}^t \cdot (\mathbf{L}^t + \boldsymbol{\tau}_X^t)} |\mathbf{L}^t + \boldsymbol{\tau}_X^t\rangle,\end{aligned}\quad (7)$$

where  $N$  is the normalization factor,  $\mathbf{L}^{b/t} = n_1 \mathbf{a}_1^{b/t} + n_2 \mathbf{a}_2^{b/t}$  is the unit cell vector, and  $|\mathbf{L}^{b/t} + \boldsymbol{\tau}_X^{b/t}\rangle$  denotes the  $p_z$  orbital located at sublattice  $X$  in unit cell  $\mathbf{L}^{b/t}$ . The intralayer Hamiltonian matrix element reads

$$\begin{aligned}\langle \mathbf{k}^b, X | H_0 | \mathbf{k}^{b'}, X' \rangle &= \delta_{\mathbf{k}^b \mathbf{k}^{b'}} \sum_{\mathbf{L}^b} t(\mathbf{L}^b + \boldsymbol{\tau}_{X'X}^b) e^{i\mathbf{k}^b \cdot (\mathbf{L}^b + \boldsymbol{\tau}_{X'X}^b)}, \\ \langle \mathbf{k}^t, X | H_0 | \mathbf{k}^{t'}, X' \rangle &= \delta_{\mathbf{k}^t \mathbf{k}^{t'}} \sum_{\mathbf{L}^t} t(\mathbf{L}^t + \boldsymbol{\tau}_{X'X}^t) e^{i\mathbf{k}^t \cdot (\mathbf{L}^t + \boldsymbol{\tau}_{X'X}^t)},\end{aligned}\quad (8)$$

where  $\boldsymbol{\tau}_{X'X}^{b/t} = \boldsymbol{\tau}_{X'}^{b/t} - \boldsymbol{\tau}_X^{b/t}$ . The interlayer Hamiltonian matrix element reads [16,23–28]

$$\langle \mathbf{k}^b, X | U | \mathbf{k}^t, X' \rangle = \sum_{\mathbf{G}^b \mathbf{G}^t} T(\mathbf{k}^b + \mathbf{G}^b) e^{i\mathbf{G}^b \cdot \boldsymbol{\tau}_X^b} e^{-i\mathbf{G}^t \cdot \boldsymbol{\tau}_{X'}^t} \delta_{\mathbf{k}^b + \mathbf{G}^b, \mathbf{k}^t + \mathbf{G}^t}, \quad (9)$$

where  $T(\mathbf{k}^b + \mathbf{G}^b)$  is the in-plane Fourier transform of the interlayer hopping function  $t(\mathbf{r})$  at  $\mathbf{k}^b + \mathbf{G}^b$ . It is defined by

$$T(\mathbf{q}) = \frac{1}{S} \int t(\mathbf{r}_{xy} + h\hat{\mathbf{e}}_z) e^{-i\mathbf{q} \cdot \mathbf{r}_{xy}} d\mathbf{r}_{xy}, \quad (10)$$

where  $S$  is the area of the unit cell of hexagon or square lattice, and  $\hat{\mathbf{e}}_z$  is the unit vector along  $z$  axis. According to Eq. (9), only Bloch bases with the wave vectors  $\mathbf{k}^b$  and  $\mathbf{k}^t$  satisfying  $\mathbf{k}^b + \mathbf{G}^b = \mathbf{k}^t + \mathbf{G}^t$  can couple with each other, where  $\mathbf{G}^b$  and  $\mathbf{G}^t$  are the reciprocal point vectors of the two layers.

These resonant  $\mathbf{k}^b$  and  $\mathbf{k}^t$  points are labeled as  $\mathbf{Q}_i(\mathbf{k}_0)$  with even and odd  $i$  belonging to the bottom and top layers, respectively, in which wave vectors  $\mathbf{Q}_i$  are determined by the interlayer coupling strengths in Eq. (10). In this paper we focus on these  $\mathbf{Q}_i$ , which lead to the first two strongest interlayer coupling strengths. At  $\Gamma$  point, i.e.,  $\mathbf{k}_0 = 0$ , the coordinates of these  $\mathbf{Q}_i$  determined by Eq. (10) in dodecagonal and octagonal vdW-QCs are given in Table I. For  $\mathbf{k}_0 \neq 0$ , these wave vectors  $\mathbf{Q}_i(\mathbf{k}_0)$  have a corresponding translational motion of  $\mathbf{k}_0$  with respect to  $\mathbf{Q}_i$  at  $\mathbf{k}_0 = 0$ , as shown in Figs. 2 and 3. In general, the resonant coupling Hamiltonian  $H(\mathbf{k}_0)$  for vdW-QCs within the subspace consisting of  $\mathbf{Q}_i$  can be

TABLE I. First two strongest coupling strengths  $T_0$  with their wave vectors  $\mathbf{Q}_i$  in dodecagonal (dode) and octagonal (octa) vdW-QCs. The coordinate of wave vector  $\mathbf{Q}_i$  is determined by  $\mathbf{Q}_i = (-1)^i R(\frac{\pi}{n})\mathbf{Q}_0$  with  $i = 0, 1, 2, \dots, n-1$ . Here  $\mathbf{Q}_i$  with even and odd  $i$  belong to the top and bottom layers, respectively.

Systems	Order	Symmetries	$\mathbf{Q}_0$	$T_0$
dode	first	$\mathbb{D}_{6d}$	$(\frac{4\pi}{\sqrt{3}a}, 0)$	$0.047\gamma_0$
dode	second	$\mathbb{D}_{2d}$	$(\frac{2\pi}{\sqrt{3}a} - \frac{2\pi}{a}, 0)$	$0.014\gamma_0$
octa	first	$\mathbb{D}_{4d}$	$(\frac{\pi}{(\sqrt{2+1}a)}, \frac{\pi}{a})$	$-0.0296\gamma_0$
octa	second	$\mathbb{D}_{4d}$	$(\frac{(\sqrt{2-2}\pi)}{a}, \frac{\sqrt{2}\pi}{a})$	$0.0024\gamma_0$

written as

$$H(\mathbf{k}_0) = H_0^b(\mathbf{k}_0) + H_0^t(\mathbf{k}_0) + U(\mathbf{k}_0), \quad (11)$$

where  $H_0^b(\mathbf{k}_0)$  and  $H_0^t(\mathbf{k}_0)$  are the Hamiltonians of the two component layers, and  $U(\mathbf{k}_0)$  is the interlayer coupling. The matrix elements for  $H_0^b(\mathbf{k}_0)$  and  $H_0^t(\mathbf{k}_0)$  are determined by Eq. (8), and the matrix elements for  $U(\mathbf{k}_0)$  are determined by Eq. (9). The eigenenergy  $E(\mathbf{k}_0)$  of  $H(\mathbf{k}_0)$  as a function of  $\mathbf{k}_0$  is called as the quasiband structure and can well describe electronic properties of vdW-QCs [16].

## IV. SYMMETRIES OF RESONANT COUPLING HAMILTONIANS

### A. The first strongest resonant coupling in dodecagonal vdW-QC

We first consider the resonant coupling for  $\mathbf{k}_0 = 0$  in Fig. 2(b) and later discuss the other cases for  $\mathbf{k}_0 \neq 0$ . For the first strongest resonant coupling, there are 12 wave vectors  $\mathbf{Q}_i$  ranging from  $\mathbf{Q}_0$  to  $\mathbf{Q}_{11}$  with their coordinates given in Table I. These 12 wave vectors  $\mathbf{Q}_i$  have the same coupling energy between  $\mathbf{Q}_i$  and  $\mathbf{Q}_{i+1}$  (or  $\mathbf{Q}_{i-1}$ ) with  $0.047\gamma_0$  in the dodecagonal vdW-QC. The couplings between other two  $\mathbf{Q}_i$  points are very weak and hence are neglected. We adopt the sublattice order for  $\mathbf{Q}_n$  as (A, B) if  $n \bmod 4 = 2, 3$  and (B, A) if  $n \bmod 4 = 0, 1$ , and then write the Hamiltonian at  $\Gamma$  point as

$$H_\Gamma = \begin{pmatrix} H^{(0)} & W_{0,1} & & & & & & & & & & W_{11,0}^\dagger \\ W_{0,1}^\dagger & H^{(1)} & W_{1,2} & & & & & & & & & & \\ & W_{1,2}^\dagger & H^{(2)} & \ddots & & & & & & & & & \\ & & & \ddots & \ddots & & & & & & & & \\ & & & & W_{9,10}^\dagger & & & & & & & & \\ W_{11,0} & & & & & W_{9,10} & H^{(10)} & & & & & & \\ & & & & & & W_{10,11}^\dagger & & & & & & \\ & & & & & & & W_{10,11} & H^{(11)} & & & & \end{pmatrix}. \quad (12)$$

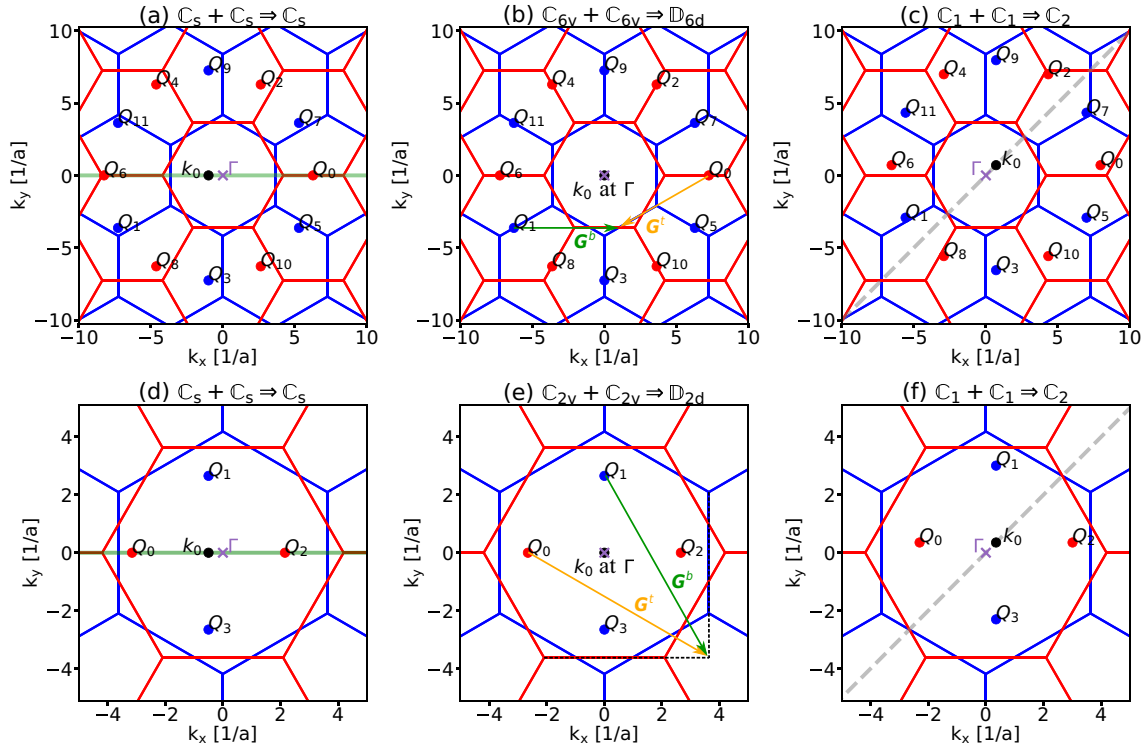


FIG. 2. Wave vectors  $\mathbf{Q}_i$  for the (first, second) strongest resonant coupling in dodecagonal vdW-QC for (a) and (d)  $\mathbf{k}_0$  shifting away from  $\Gamma$  along  $-\mathbf{k}_x$  direction, (b) and (e)  $\mathbf{k}_0$  at  $\Gamma$ , and (c) and (f)  $\mathbf{k}_0$  shifting equivalently away from  $\Gamma$  along  $\Gamma O_0$  direction [also see Fig. 1(c)]. Wave vectors  $\mathbf{Q}_i$  with odd and even  $i$  belong to the bottom and top layers, respectively. The reflection mirrors for  $C_s$  point group symmetry in (a) and (d) are denoted by green solid lines. The twofold axes for  $C_2$  point group symmetry in (c) and (f) are denoted by gray dashed lines. In (b) and (e), the interlayer coupling conditions between  $\mathbf{Q}_0$  and  $\mathbf{Q}_1$  are depicted, namely  $\mathbf{Q}_0 + \mathbf{G}^t = \mathbf{Q}_1 + \mathbf{G}^b$ . Blue and red hexagon networks are the BZs of the bottom and top layers of dodecagonal vdW-QCs in each subplot.

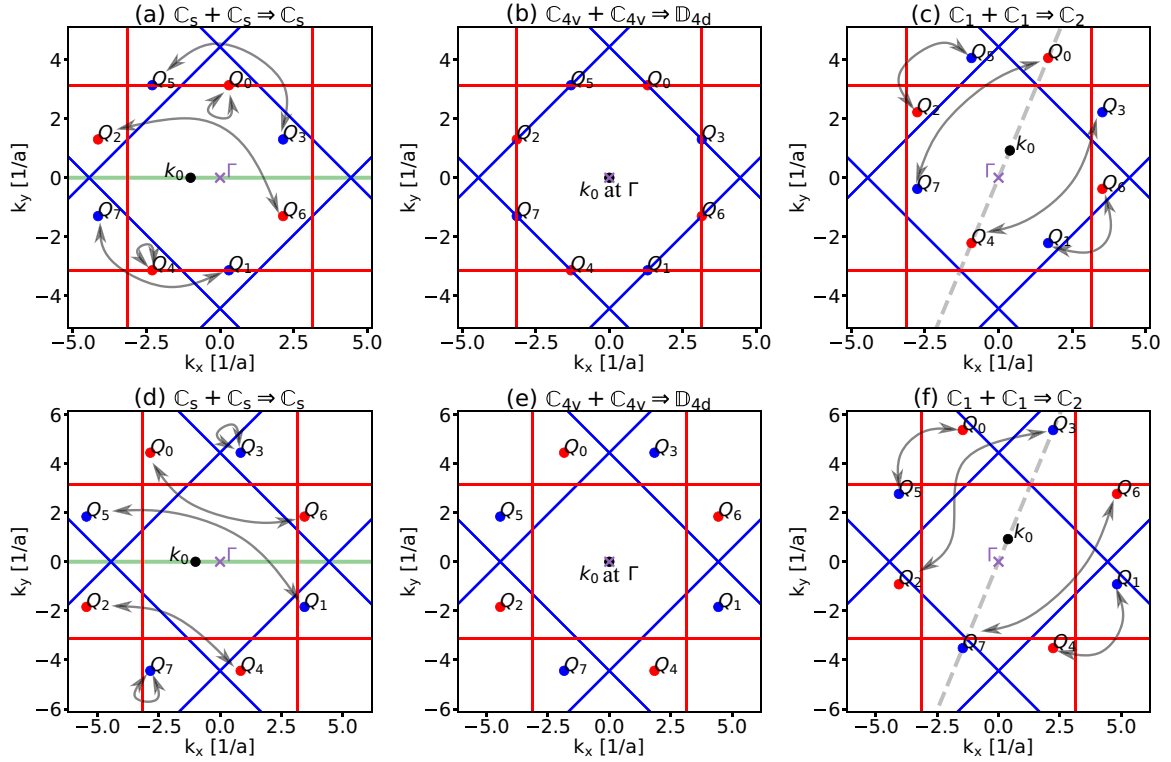


FIG. 3. Wave vectors  $\mathbf{Q}_i$  for the (first, second) strongest resonant coupling in octagonal vdW-QC for (a) and (d)  $\mathbf{k}_0$  shifting away from  $\Gamma$  along  $-\mathbf{k}_x$  direction, (b) and (e)  $\mathbf{k}_0$  at  $\Gamma$ , and (c) and (f)  $\mathbf{k}_0$  shifting equivalently away from  $\Gamma$  along  $\Gamma O_0$  direction [also see Fig. 1(d)]. Wave vectors  $\mathbf{Q}_i$  with odd and even  $i$  belong to the bottom and top layers, respectively. The reflection mirrors  $\sigma_x$  for  $C_s$  point group in (a) and (d) are denoted by green solid lines. The twofold axes  $\Gamma O_0$  of  $C_{2,\Gamma O_0}$  for  $C_2$  point group in (c) and (f) are denoted by gray dashed lines. Blue and red hexagon networks are the BZs of the bottom and top layers of dodecagonal vdW-QCs in each subplot. These  $\mathbf{Q}_i$  points connected by  $\sigma_x$  in (a) and (d) and these  $\mathbf{Q}_i$  points connected by  $C_{2,\Gamma O_0}$  are denoted as curved lines with double arrows.

Here  $H^{(n)}$  is the Hamiltonian at the  $n$ th  $k$  point with the same form

$$H^{(n)} = \gamma_0 \begin{pmatrix} 0.239 & 0.682 \\ 0.682 & 0.239 \end{pmatrix}, \quad (13)$$

and  $W_{n,n+1}$  is the interlayer interaction between the  $n$ th and  $(n+1)$ th  $k$  points with the same form

$$W_{n,n+1} = T_0 \begin{pmatrix} e^{\frac{2\pi}{3}i} & 1 \\ 1 & e^{-\frac{2\pi}{3}i} \end{pmatrix}, \quad (14)$$

where  $T_0 = 0.047\gamma_0$  is the interlayer coupling strength between  $\mathbf{Q}_i$  and  $\mathbf{Q}_{i+1}$ . This Hamiltonian  $H_\Gamma$  has  $\mathbb{D}_{6d}$  point group symmetry, which is the same as that for BZs of dodecagonal vdW-QC as shown in Fig. 1(c) but with following symmetry operations [17]:

$$\begin{aligned} E &= I(\mathbf{k}) \otimes \sigma_0, \\ S_{12}^{2i+1} &= S_{12}^{2i+1}(\mathbf{k}) \otimes \sigma_0 \quad (i = 0, 1, \dots, 5), \\ C_{12}^{2i} &= C_{12}^{2i}(\mathbf{k}) \otimes \sigma_0 \quad (i = 1, 2, \dots, 5), \\ C'_{2,i} &= C'_{2,i}(\mathbf{k}) \otimes \sigma_1 \quad (i = 0, 1, \dots, 5), \\ \sigma_{d,i} &= \sigma_{d,i}(\mathbf{k}) \otimes \sigma_1 \quad (i = 0, 1, \dots, 5). \end{aligned} \quad (15)$$

All of these symmetry operations are the direct product of the operations in  $\mathbf{k}$  space and the operations in sublattice space. Symmetry operations  $I(\mathbf{k})$ ,  $S_{12}^{2i+1}(\mathbf{k})$ ,  $C_{12}^{2i}(\mathbf{k})$ ,  $C'_{2,i}(\mathbf{k})$ ,

and  $\sigma_{d,i}(\mathbf{k})$  are  $12 \times 12$  matrices within the space of 12 wave vectors  $\mathbf{Q}_i$ . These  $\mathbf{k}$ -space operations can be described by Eq. (2) with  $n = 6$ . Here operations  $\sigma_0$  and  $\sigma_1$  are the identity matrix  $I$  and the  $x$  component of Pauli matrices in sublattice space, respectively.

If  $\mathbf{k}_0$  shifts away from  $\Gamma$  point along  $-\mathbf{k}_x$  direction, which is equivalent to the case that  $\mathbf{k}_0$  moves along arbitrary  $\Gamma \rightarrow K_i^{b/t}$  direction [the green solid lines in Fig. 1(c)], only the symmetry operation  $\sigma_{d,0}$  (i.e.,  $\sigma_x$ ) in point group  $\mathbb{D}_{6d}$  is kept. In this case, the symmetry of the Hamiltonian decrease to be  $C_s$  point group including  $E$  and  $\sigma_x$ , as shown in Fig. 2(a).

If  $\mathbf{k}_0$  shifts away from  $\Gamma$  along  $\Gamma \rightarrow O_0$  direction, which is equivalent to the case that  $\mathbf{k}_0$  moves along arbitrary  $\Gamma \rightarrow O_i$  direction [the gray dashed lines in Fig. 1(c)], only one twofold rotation  $C'_{2,1}$  in  $\mathbb{D}_{6d}$ , labeled by  $C_{2,\Gamma O_0}$  with  $\Gamma \rightarrow O_0$  as the rotation axis, is kept. In this case, the symmetry decrease from  $\mathbb{D}_{6d}$  to  $C_2$  point group including  $E$  and  $C_{2,\Gamma O_0}$ , as shown in Fig. 2(c).

## B. The second strongest resonant coupling in dodecagonal vdW-QC

For the second strongest resonant coupling, there are only four wave vectors  $\mathbf{Q}_i$  supporting the subspace with their coordinates in Table I. We label  $\mathbf{Q}_0$  and  $\mathbf{Q}_2$  from the top layer, and  $\mathbf{Q}_1$  and  $\mathbf{Q}_3$  from the bottom layer in Fig. 2(e). The Hamiltonian

$H_\Gamma$  at  $\Gamma$  point for the second strongest resonant coupling reads

$$H_\Gamma = \begin{pmatrix} H^{(0)} & W_{0,1} & 0 & W_{3,0}^\dagger \\ W_{0,1}^\dagger & H^{(1)} & W_{1,2} & 0 \\ 0 & W_{1,2}^\dagger & H^{(2)} & W_{2,3} \\ W_{3,0} & 0 & W_{2,3}^\dagger & H^{(3)} \end{pmatrix}. \quad (16)$$

Here the sublattice order is arranged as  $(A, B)$  for  $\mathcal{Q}_0$  and  $\mathcal{Q}_3$  and  $(B, A)$  for  $\mathcal{Q}_1$  and  $\mathcal{Q}_2$ , the matrix elements in the Hamiltonian take the form

$$H^{(n)} = \gamma_0 \begin{pmatrix} 0.083 & 1.433 \\ 1.433 & 0.083 \end{pmatrix} \quad (17)$$

and

$$W_{n,n+1} = T_0 \begin{pmatrix} e^{\frac{2\pi}{3}i} & 1 \\ 1 & e^{-\frac{2\pi}{3}i} \end{pmatrix}, \quad (18)$$

where  $T_0 = 0.014\gamma_0$  is the interlayer coupling strength between  $\mathcal{Q}_i$  and  $\mathcal{Q}_{i+1}$ . The Hamiltonian in Eq. (16) has  $\mathbb{D}_{2d}$  point group symmetry with the  $z$  axis being the principal axis, and the symmetry operations read

$$\begin{aligned} E &= I(\mathbf{k}) \otimes \sigma_0, \\ S_4^i &= S_4^i(\mathbf{k}) \otimes \sigma_0 \quad (i = 1, 3), \\ C_2^1 &= C_2^1(\mathbf{k}) \otimes \sigma_0, \\ C_{2,i}' &= C_{2,i}'(\mathbf{k}) \otimes \sigma_1 \quad (i = 0, 1), \\ \sigma_{d,i} &= \sigma_{d,i}(\mathbf{k}) \otimes \sigma_1 \quad (i = 0, 1), \end{aligned} \quad (19)$$

where the operations  $I(\mathbf{k})$ ,  $S_4^i(\mathbf{k})$ ,  $C_2^1(\mathbf{k})$ ,  $C_{2,i}'(\mathbf{k})$ , and  $\sigma_{d,i}(\mathbf{k})$  are  $4 \times 4$  matrices acting on the  $\mathbf{k}$  space of  $\mathcal{Q}_i$  ranging from  $\mathcal{Q}_0$  to  $\mathcal{Q}_3$ , which satisfy Eq. (2) with  $n = 2$ . Similar to the first strongest resonant coupling, if  $\mathbf{k}_0$  shifts away from  $\Gamma$  along  $-\mathbf{k}_x$  and  $\Gamma \rightarrow O_0$  directions, only the symmetry operations  $\sigma_x$  and  $C_{2,\Gamma O_0}$  are kept, respectively. In this way, the symmetries the Hamiltonian correspondingly decrease to be  $\mathbb{C}_s$  and  $\mathbb{C}_2$ , as shown in Figs. 2(d) and 2(f).

### C. First two strongest resonant couplings in octagonal vdW-QC

For both the first two strongest couplings [11], there are eight wave vectors  $\mathcal{Q}_i$  ( $i = 0, 1, \dots, 7$ ) with their coordinates given in Table I. These wave vectors  $\mathcal{Q}_i$  for even and odd  $i$  belong to the top and bottom layers, respectively. The strongest interactions occur between  $\mathcal{Q}_i$  and  $\mathcal{Q}_{i+1}$  with the coupling conditions  $\mathcal{Q}_{2i} + \mathbf{G}^i = \mathcal{Q}_{2i+1}$  and  $\mathcal{Q}_{2i-1} + \mathbf{G}^b = \mathcal{Q}_{2i}$ , where  $\mathbf{G}^b$  and  $\mathbf{G}^i$  are some special reciprocal points with  $|\mathbf{G}^i| = |\mathbf{G}^b|$  being  $\frac{2\pi}{a}$  and  $\frac{2\sqrt{2}\pi}{a}$  for the first strongest and the second strongest resonant coupling, respectively, in Figs. 3(b) and 3(e). The resonant coupling Hamiltonian at  $\Gamma$  point reads

$$H_\Gamma = \begin{pmatrix} h_0 & T_0 & & & & & & T_0 \\ T_0 & h_1 & T_0 & & & & & \\ & T_0 & h_2 & \cdots & & & & \\ & & \cdots & \cdots & T_0 & & & \\ & & & T_0 & h_6 & T_0 & & \\ T_0 & & & & T_0 & h_7 & & \end{pmatrix}, \quad (20)$$

where the on-site energy  $h_i$  for all  $\mathcal{Q}_i$  sites take the same value  $0.158\gamma_0$  ( $0.105\gamma_0$ ) and hopping energy  $T_0$  between  $\mathcal{Q}_i$  and

$\mathcal{Q}_{i+1}$  is  $-0.0296\gamma_0$  ( $0.0024\gamma_0$ ) for the first (second) strongest resonant coupling. As shown in Figs. 3(b) and 3(e), this Hamiltonian has  $\mathbb{D}_{4d}$  point group symmetry with the principle  $z$  axis, which is the same as the BZs of octagonal vdW-QC as shown in Fig. 1(d). The symmetry operations include rotations  $C_4^i$ , improper rotations  $S_8^{2i+1}$ , reflections  $\sigma_{d,i}$ , and twofold rotations  $C_{2,i}'$  with  $i = 0, 1, 2, 3$ . These symmetry operations satisfy Eqs. (2) and (3) with  $n = 4$  with only one sublattice. If  $\mathbf{k}_0$  shifts away from  $\Gamma$  along  $-\mathbf{k}_x$  direction, only the reflection  $\sigma_x$  is kept, and then the Hamiltonian has a lower  $\mathbb{C}_s$  point group symmetry in Figs. 3(a) and 3(d). If  $\mathbf{k}_0$  shifts away from  $\Gamma$  along  $\Gamma \rightarrow O_0$  direction, the Hamiltonian has  $\mathbb{C}_2$  point group symmetry in Figs. 3(c) and 3(f).

However, here we figure out that the reflections in Figs. 3(a) and 3(d) and the twofold rotations in Figs. 3(c) and 3(f) act on these  $\mathcal{Q}_i$  points in a different way from them acting on a real-space molecule structure. Let us first take  $\sigma_x$  (i.e.,  $\sigma_{d,0}$ ) in Fig. 3(a) for the first strongest resonant coupling as an example. Under the  $\sigma_x$  operation, red  $\mathcal{Q}_0$  is reflected into the position where blue  $\mathcal{Q}_1$  is located in the  $xy$  plane. Blue  $\mathcal{Q}_1$  is at the bottom layer, and hence blue  $\mathcal{Q}_1$  is not directly the point reflected by  $\sigma_x$  for red  $\mathcal{Q}_0$  from the top layer. However, a red point at the same place of blue  $\mathcal{Q}_1$  but for the top layer stands for the same state of the red  $\mathcal{Q}_0$  because of a reciprocal point vector difference. Therefore,  $\sigma_x$  will reflect  $\mathcal{Q}_0$  to itself. The same way  $\sigma_x$  acts on the other  $\mathcal{Q}_i$ , and these  $\mathcal{Q}_i$  points reflected by  $\sigma_x$  are denoted by curved lines with double arrows in Fig. 3(a) for the first strongest resonant coupling and similarly in Fig. 3(d) for the second strongest resonant coupling.

For the operation  $C_{2,\Gamma O_0}$  in Figs. 3(c) and 3(f), we can also perform a similar analysis. For example, under the  $C_{2,\Gamma O_0}$  operation in Fig. 3(c), red  $\mathcal{Q}_0$  will be rotated to a blue  $\mathbf{k}$  point at the same place as the red  $\mathcal{Q}_0$  in the  $xy$  plane. Owing to a reciprocal point vector difference, the blue  $\mathcal{Q}_7$  stand for the same state of the blue  $\mathbf{k}$  point at the same place as the red  $\mathcal{Q}_0$ . Therefore, blue  $\mathcal{Q}_7$  is the point for red  $\mathcal{Q}_0$  under  $C_{2,\Gamma O_0}$ . The same way of  $C_{2,\Gamma O_0}$  acts on the other  $\mathcal{Q}_i$ , and these  $\mathcal{Q}_i$  points connected by  $C_{2,\Gamma O_0}$  are denoted by curved lines with double arrows in Fig. 3(c) for the first strongest resonant coupling and similarly in Fig. 3(f) for the second strongest resonant coupling.

## V. COMPATIBILITY RELATIONSHIP FOR QUASIBAND SPLITS

### A. Dodecagonal vdW-QC

As previously discussed in Figs. 2(a)–2(c), at  $\Gamma$  point, the first strongest resonant coupling Hamiltonian  $H_\Gamma$  in dodecagonal vdW-QC has the highest  $\mathbb{D}_{6d}$  point group symmetry, while for  $\mathbf{k}_0$  along  $-\mathbf{k}_x$  and  $\Gamma \rightarrow O_0$  directions, the Hamiltonians  $H(\mathbf{k}_0)$  have  $\mathbb{C}_s$  and  $\mathbb{C}_2$  point group symmetries, respectively. Therefore, if  $\mathbf{k}_0$  deviates from  $\Gamma$  point, the original two-dimensional degenerate  $E_i$  states at  $\Gamma$  point in  $\mathbb{D}_{6d}$  symmetry will be split into one-dimensional nondegenerate states due to the decreased symmetry. Using the character tables of  $\mathbb{D}_{6d}$ ,  $\mathbb{C}_s$ , and  $\mathbb{C}_2$  in Table II, we derive the CR between  $\mathbb{D}_{6d}$  and  $\mathbb{C}_s$  and the CR between  $\mathbb{D}_{6d}$  and  $\mathbb{C}_2$ , as also listed in Table II for comparison. From the CRs in Table II, we can see that (i) as  $\mathbb{D}_{6d}$  is broken into  $\mathbb{C}_s$  along  $-\mathbf{k}_x$  direction, we have  $A_1 \rightarrow A'$ ,

TABLE II. Character tables of  $\mathbb{D}_{6d}$ ,  $\mathbb{C}_s$ , and  $\mathbb{C}_2$  point groups and their CRs.

$\mathbb{C}_2$	$\mathbb{C}_s$	$\mathbb{D}_{6d}$	$E$							$\mathbb{C}_{2,\Gamma O_0}$		
			$E$	$2S_{12}$	$2C_6$	$2S_4$	$2C_3$	$2S_{12}^5$	$C_2$	$6C_2'$	$\sigma_x$ $6\sigma_d$	
$A$	$A'$	$A_1$	1	1	1	1	1	1	1	1	1	1
$B$	$A''$	$A_2$	1	1	1	1	1	1	1	1	-1	-1
$A$	$A''$	$B_1$	1	-1	1	-1	1	-1	1	1	1	-1
$B$	$A'$	$B_2$	1	-1	1	-1	1	-1	1	1	-1	1
$A \oplus B$	$A' \oplus A''$	$E_1$	2	$\sqrt{3}$	1	0	-1	$-\sqrt{3}$	-2	0	0	0
$A \oplus B$	$A' \oplus A''$	$E_2$	2	1	-1	-2	-1	1	2	0	0	0
$A \oplus B$	$A' \oplus A''$	$E_3$	2	0	-2	0	2	0	-2	0	0	0
$A \oplus B$	$A' \oplus A''$	$E_4$	2	-1	-1	2	-1	-1	2	0	0	0
$A \oplus B$	$A' \oplus A''$	$E_5$	2	$-\sqrt{3}$	1	0	-1	$\sqrt{3}$	-2	0	0	0

$A_2 \rightarrow A''$ ,  $B_1 \rightarrow A''$ , and  $B_2 \rightarrow A'$  for nondegenerate states, and have  $E_i \rightarrow A' \oplus A''$  with  $i = 1, \dots, 5$  for degenerate  $E_i$  states; and (ii) as  $\mathbb{D}_{6d}$  is broken into  $\mathbb{C}_2$  along  $\Gamma \rightarrow O_0$  direction, we have  $A_1 \rightarrow A$ ,  $A_2 \rightarrow B$ ,  $B_1 \rightarrow A$ , and  $B_2 \rightarrow B$  for nondegenerate states, and have  $E_i \rightarrow A \oplus B$  with  $i = 1, \dots, 5$  for degenerate  $E_i$  states.

Similarly, for the second strongest resonant coupling in Figs. 2(d)–2(f), using the character tables of  $\mathbb{D}_{2d}$ ,  $\mathbb{C}_s$ , and  $\mathbb{C}_2$  in Table III, we derive the CR between  $\mathbb{D}_{2d}$  and  $\mathbb{C}_s$  and the CR between  $\mathbb{D}_{2d}$  and  $\mathbb{C}_2$ , as also listed in Table III for comparison. From the CRs in Table III, we can see that (i) as  $\mathbb{D}_{2d}$  is broken into  $\mathbb{C}_s$  along  $-\mathbf{k}_x$  direction, we have  $A_1 \rightarrow A'$ ,  $A_2 \rightarrow A''$ ,  $B_1 \rightarrow A''$ , and  $B_2 \rightarrow A'$  for nondegenerate states, and have  $E \rightarrow A' \oplus A''$  for degenerate  $E$  states; and (ii) as  $\mathbb{D}_{6d}$  is broken into  $\mathbb{C}_2$  along  $\Gamma \rightarrow O_0$  direction, we have  $A_1 \rightarrow A$ ,  $A_2 \rightarrow B$ ,  $B_1 \rightarrow A$ , and  $B_2 \rightarrow B$  for nondegenerate states, and have  $E \rightarrow A \oplus B$  for degenerate  $E$  states.

On the other hand, substituting the Hamiltonian matrix elements in Eqs. (8) and (9) into the Hamiltonian  $H(\mathbf{k}_0)$  in Eq. (11) for the first and second strongest resonant couplings in dodecagonal vdW-QC, we numerically obtain their quasiband structures as a function of  $\mathbf{k}_0$  and plot the results in Fig. 4. We clearly see the symmetry changes and band splits predicted by the CRs in Tables II and III.

### B. Octagonal vdW-QC

Both the first and second strongest resonant coupling Hamiltonians at  $\Gamma$  point in octagonal vdW-QC have the highest  $\mathbb{D}_{4d}$  point group symmetry, as shown in Figs. 3(b) and 3(e). For  $\mathbf{k}_0$  along  $-\mathbf{k}_x$  and  $\Gamma \rightarrow O_0$  directions, the Hamiltonians

TABLE III. Character tables of  $\mathbb{D}_{2d}$ ,  $\mathbb{C}_s$ , and  $\mathbb{C}_2$  point groups and their CRs.

$\mathbb{C}_2$	$\mathbb{C}_s$	$\mathbb{D}_{2d}$	$E$				$\mathbb{C}_{2,\Gamma O_0}$	
			$E$	$2S_4$	$C_2$	$2C_2'$	$\sigma_x$ $2\sigma_d$	
$A$	$A'$	$A_1$	1	1	1	1	1	
$B$	$A''$	$A_2$	1	1	1	-1	-1	
$A$	$A''$	$B_1$	1	-1	1	1	-1	
$B$	$A'$	$B_2$	1	-1	1	-1	1	
$A \oplus B$	$A' \oplus A''$	$E$	2	0	-2	0	0	

$H(\mathbf{k}_0)$  have  $\mathbb{C}_s$  and  $\mathbb{C}_2$  point group symmetries, respectively. Using the character tables of  $\mathbb{D}_{4d}$ ,  $\mathbb{C}_s$ , and  $\mathbb{C}_2$  in Table IV, we derive the CR between  $\mathbb{D}_{4d}$  and  $\mathbb{C}_s$  and the CR between  $\mathbb{D}_{4d}$  and  $\mathbb{C}_2$ , as also listed in Table IV for comparison. From the CRs in Table IV, we can see that (i) as  $\mathbb{D}_{4d}$  is broken into  $\mathbb{C}_s$  along  $-\mathbf{k}_x$  direction, we have  $A_1 \rightarrow A'$ ,  $A_2 \rightarrow A''$ ,  $B_1 \rightarrow A''$ , and  $B_2 \rightarrow A'$  for nondegenerate states, and have  $E_i \rightarrow A' \oplus A''$  with  $i = 1, 2, 3$  for degenerate  $E_i$  states; and (ii) as  $\mathbb{D}_{4d}$  is broken into  $\mathbb{C}_2$  along  $\Gamma \rightarrow O_0$  direction, we have  $A_1 \rightarrow A$ ,  $A_2 \rightarrow B$ ,  $B_1 \rightarrow A$ , and  $B_2 \rightarrow B$  for nondegenerate states, and have  $E_i \rightarrow A \oplus B$  with  $i = 1, 2, 3$  for degenerate  $E_i$  states. The numerically calculated quasiband structures as a function of  $\mathbf{k}_0$  in Fig. 5 verify the symmetry changes and band splits predicted by the CRs in Table IV.

### VI. IHSRS IN $k$ SPACE

The interlayer hybridization is important because it is responsible for the unique properties of vdW-QCs distinct from those of component monolayers. In our previous work we proposed the IHSRs for the symmetry restriction  $\mathbb{C}_{6v} + \mathbb{C}_{6v} \Rightarrow \mathbb{D}_{6d}$  in graphene quasicrystal systems by using projection operator analysis [17]. The interlayer hybridizations are classified into three categories, (1) *equivalent hybridization*, if the allowed pairing states from two monolayers for interlayer hybridizations have the same irreducible representations, (2) *nonequivalent hybridization*, if the allowed pairing states from two monolayers for interlayer hybridizations only have different irreducible representations, and (3) *mixed hybridization*, if the allowed pairing states from two monolayers for interlayer

TABLE IV. Character tables of  $\mathbb{D}_{4d}$ ,  $\mathbb{C}_s$ , and  $\mathbb{C}_2$  point groups and their CRs.

$\mathbb{C}_2$	$\mathbb{C}_s$	$\mathbb{D}_{4d}$	$E$					$\mathbb{C}_{2,\Gamma O_0}$		
			$E$	$2S_8$	$2C_4$	$2S_8^3$	$C_2$	$4C_2'$	$\sigma_x$ $4\sigma_d$	
$A$	$A'$	$A_1$	1	1	1	1	1	1	1	1
$B$	$A''$	$A_2$	1	1	1	1	1	1	-1	-1
$A$	$A''$	$B_1$	1	-1	1	-1	1	1	1	-1
$B$	$A'$	$B_2$	1	-1	1	-1	1	1	-1	1
$A \oplus B$	$A' \oplus A''$	$E_1$	2	$\sqrt{2}$	0	$-\sqrt{2}$	-2	0	0	0
$A \oplus B$	$A' \oplus A''$	$E_2$	2	0	-2	0	2	0	0	0
$A \oplus B$	$A' \oplus A''$	$E_3$	2	$-\sqrt{2}$	0	$\sqrt{2}$	-2	0	0	0

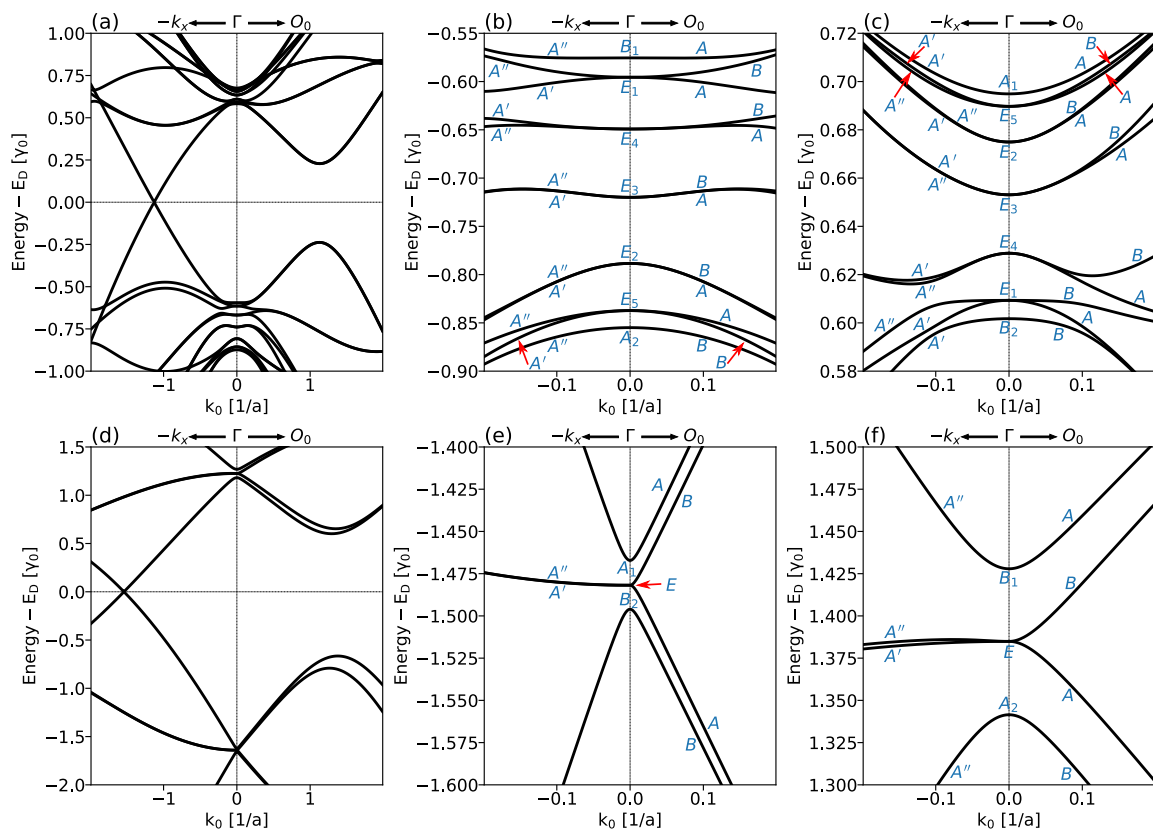


FIG. 4. (a) and (d) The quasiband structures of the dodecagonal vdW-QC for the (first, second) strongest resonant couplings with Dirac point  $E_D$  as energy reference. (b) and (c) Zoom-in images of (a) with irreducible representations in negative and positive energy regions around  $\Gamma$  point. (e) and (f) Zoom-in images of (d) with irreducible representations in negative and positive energy regions around  $\Gamma$  point.

hybridizations can have the same and different irreducible representations. Here we alternatively use the CRs of different point groups to derive the IHSRs of both the first and second strongest resonant couplings in  $k$  space for dodecagonal and octagonal vdW-QCs.

### A. IHSRs at $\Gamma$ point

There are 12 wave vectors  $\mathcal{Q}_i$  forming the  $\mathbb{D}_{6d}$  subspace for the first strongest resonant coupling at  $\Gamma$  point in Fig. 2(b) for dodecagonal vdW-QC. The six  $\mathcal{Q}_i$  with even  $i$  form the

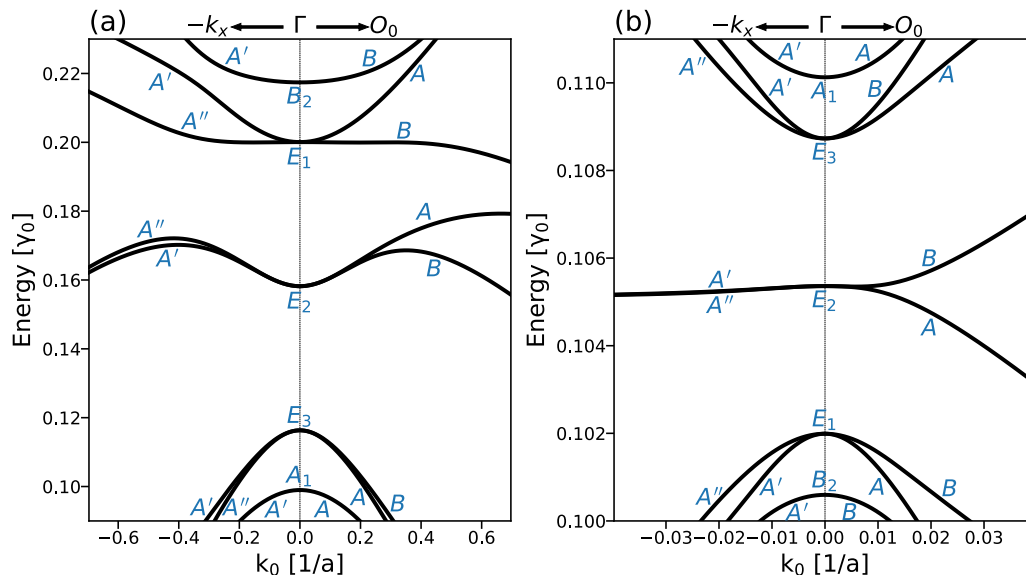


FIG. 5. The quasiband structures of the octagonal vdW-QC around  $\Gamma$  point with irreducible representations for (a) the first and (b) second strongest resonant couplings.



TABLE V. Character tables of  $\mathbb{D}_{6d}$ ,  $\mathbb{C}_{6v}^b$ , and  $\mathbb{C}_{6v}^t$  point groups and their CRs.  $3\sigma_v^b/3\sigma_d^b$  and  $3\sigma_d^t/3\sigma_v^t$  respectively stand for the two classes  $\{\sigma_{v,i}^b\}$  and  $\{\sigma_{d,i}^b\}$  in  $\mathbb{C}_{6v}^b$  and the two classes  $\{\sigma_{d,i}^t\}$  and  $\{\sigma_{v,i}^t\}$  in  $\mathbb{C}_{6v}^t$ , with  $i = 0, 1, 2$ .

$\mathbb{C}_{6v}^t$	$\mathbb{C}_{6v}^b$	$\mathbb{D}_{6d}$	$E$		$2C_6$	$2C_3$	$C_2$	$3\sigma_d^t/3\sigma_v^t$		
			$E$	$2S_{12}$	$2C_6$	$2C_3$	$C_2$	$3\sigma_v^b/3\sigma_d^b$	$6C_2'$	
			$E$	$2S_{12}$	$2C_6$	$2S_4$	$2C_3$	$2S_{12}^5$		$6\sigma_d$
$A_1$	$A_1$	$A_1$	1	1	1	1	1	1	1	1
$A_2$	$A_2$	$A_2$	1	1	1	1	1	1	-1	-1
$A_2$	$A_2$	$B_1$	1	-1	1	-1	1	-1	1	-1
$A_1$	$A_1$	$B_2$	1	-1	1	-1	1	-1	1	1
$E_1$	$E_1$	$E_1$	2	$\sqrt{3}$	1	0	-1	$-\sqrt{3}$	-2	0
$E_2$	$E_2$	$E_2$	2	1	-1	-2	-1	1	2	0
$B_1 \oplus B_2$	$B_1 \oplus B_2$	$E_3$	2	0	-2	0	2	0	-2	0
$E_2$	$E_2$	$E_4$	2	-1	-1	2	-1	-1	2	0
$E_1$	$E_1$	$E_5$	2	$-\sqrt{3}$	1	0	-1	$\sqrt{3}$	-2	0

top  $\mathbb{C}_{6v}^t$  layer, and the six  $\mathcal{Q}_i$  with odd  $i$  form the bottom  $\mathbb{C}_{6v}^b$  layer. Due to the twist,  $\mathbb{C}_{6v}^b \neq \mathbb{C}_{6v}^t$ . Therefore, the interlayer hybridization at  $\Gamma$  point must follow the symmetry restriction  $\mathbb{C}_{6v}^b + \mathbb{C}_{6v}^t \Rightarrow \mathbb{D}_{6d}$  in dodecagonal vdW-QC. Using the character tables of  $\mathbb{D}_{6d}$ ,  $\mathbb{C}_{6v}^b$ , and  $\mathbb{C}_{6v}^t$ , we derive the CR between  $\mathbb{D}_{6d}$  and  $\mathbb{C}_{6v}^t$  and the CR between  $\mathbb{D}_{6d}$  and  $\mathbb{C}_{6v}^b$ , as listed in Table V. Using the CRs in Table V we can find the allowed interlayer hybridizations at  $\Gamma$  point for the first strongest resonant coupling in dodecagonal vdW-QC as follows:

(i) equivalent hybridizations,

$$\begin{aligned}
 A_1 + A_1 &\Rightarrow A_1 + B_2, \\
 A_2 + A_2 &\Rightarrow A_2 + B_1, \\
 E_1 + E_1 &\Rightarrow E_1 + E_5, \\
 E_2 + E_2 &\Rightarrow E_2 + E_4,
 \end{aligned} \tag{21}$$

(ii) nonequivalent hybridizations,

$$\begin{aligned}
 B_1 + B_2 &\Rightarrow E_3 + E_3, \\
 B_2 + B_1 &\Rightarrow E_3 + E_3.
 \end{aligned} \tag{22}$$

For the second strongest resonant coupling at  $\Gamma$  point in dodecagonal vdW-QC, there are four wave vectors  $\mathcal{Q}_i$  forming the  $\mathbb{D}_{2d}$  subspace with  $\mathcal{Q}_0$  and  $\mathcal{Q}_2$  from the top  $\mathbb{C}_{2v}^t$  layer and  $\mathcal{Q}_1$  and  $\mathcal{Q}_3$  from the bottom  $\mathbb{C}_{2v}^b$  layer, as shown in Fig. 2(e). Therefore, the interlayer hybridization at  $\Gamma$  point must follow the symmetry restriction  $\mathbb{C}_{2v}^b + \mathbb{C}_{2v}^t \Rightarrow \mathbb{D}_{2d}$  for the second strongest resonant coupling. Using the character tables of  $\mathbb{D}_{2d}$ ,  $\mathbb{C}_{2v}^b$ , and  $\mathbb{C}_{2v}^t$ , we derive the CR between  $\mathbb{D}_{2d}$  and  $\mathbb{C}_{2v}^t$  and the CR between  $\mathbb{D}_{2d}$  and  $\mathbb{C}_{2v}^b$ , as listed in Table VI. According to the CRs in Table VI we can obtain the allowed interlayer hybridizations at  $\Gamma$  point for the second strongest resonant coupling in dodecagonal vdW-QC as follows:

(i) equivalent hybridizations,

$$\begin{aligned}
 A_1 + A_1 &\Rightarrow A_1 + B_2, \\
 A_2 + A_2 &\Rightarrow A_2 + B_1,
 \end{aligned} \tag{23}$$

(ii) nonequivalent hybridizations,

$$\begin{aligned}
 B_1 + B_2 &\Rightarrow E + E, \\
 B_2 + B_1 &\Rightarrow E + E.
 \end{aligned} \tag{24}$$

In octagonal vdW-QC, there are eight wave vectors  $\mathcal{Q}_i$  forming the  $\mathbb{D}_{4d}$  subspace for both the first and second strongest resonant couplings at  $\Gamma$  point in Figs. 3(b) and 3(e). The four  $\mathcal{Q}_i$  with even  $i$  form the top  $\mathbb{C}_{4v}^t$  layer, and the four  $\mathcal{Q}_i$  with odd  $i$  form the bottom  $\mathbb{C}_{4v}^b$  layer. Therefore, the interlayer hybridization at  $\Gamma$  point must follow the symmetry restriction  $\mathbb{C}_{4v}^b + \mathbb{C}_{4v}^t \Rightarrow \mathbb{D}_{4d}$  in dodecagonal vdW-QC. Using the character tables of  $\mathbb{D}_{4d}$ ,  $\mathbb{C}_{4v}^b$ , and  $\mathbb{C}_{4v}^t$ , we derive the CR between  $\mathbb{D}_{4d}$  and  $\mathbb{C}_{4v}^t$  and the CR between  $\mathbb{D}_{4d}$  and  $\mathbb{C}_{4v}^b$ , as listed in Table VII. We obtain the allowed interlayer hybridizations at  $\Gamma$  point for both the first and second strongest resonant couplings in octagonal vdW-QC as follows:

(i) equivalent hybridizations,

$$\begin{aligned}
 A_1 + A_1 &\Rightarrow A_1 + B_2, \\
 A_2 + A_2 &\Rightarrow A_2 + B_1, \\
 E + E &\Rightarrow E_1 + E_3,
 \end{aligned} \tag{25}$$

(ii) nonequivalent hybridizations,

$$\begin{aligned}
 B_1 + B_2 &\Rightarrow E_2 + E_2, \\
 B_2 + B_1 &\Rightarrow E_2 + E_2.
 \end{aligned} \tag{26}$$

The interlayer hybridization matrix element is defined as  $U_{ir,ir'} = |\langle \varphi_{ir}^b | U | \varphi_{ir'}^t \rangle|$ , where  $|\varphi_{ir}^b\rangle$  and  $|\varphi_{ir'}^t\rangle$  are the states of the bottom and top layers with irreps  $ir$  and  $ir'$ . The nonzero  $U_{ir,ir'}$  represents the allowed interlayer hybridizations. From Eqs. (21)–(26) we can derive the IHSRs predicted by the CRs

TABLE VI. Character tables of  $\mathbb{D}_{2d}$ ,  $\mathbb{C}_{2v}^b$ , and  $\mathbb{C}_{2v}^t$  point groups and their CRs.  $\sigma_v^b/\sigma_d^b$  and  $\sigma_d^t/\sigma_v^t$  respectively stand for the two classes  $\{\sigma_{v,0}^b\}$  and  $\{\sigma_{d,0}^b\}$  in  $\mathbb{C}_{2v}^b$  and the two classes  $\{\sigma_{d,0}^t\}$  and  $\{\sigma_{v,0}^t\}$  in  $\mathbb{C}_{2v}^t$ .

$\mathbb{C}_{2v}^t$	$\mathbb{C}_{2v}^b$	$\mathbb{D}_{2d}$	$E$		$C_2$	$\sigma_d^t/\sigma_v^t$	
			$E$	$2S_4$	$C_2$	$\sigma_v^b/\sigma_d^b$	
			$E$	$2S_4$	$C_2$	$2C_2'$	$2\sigma_d$
$A_1$	$A_1$	$A_1$	1	1	1	1	1
$A_2$	$A_2$	$A_2$	1	1	1	-1	-1
$A_2$	$A_2$	$B_1$	1	-1	1	1	-1
$A_1$	$A_1$	$B_2$	1	-1	1	-1	1
$B_1 \oplus B_2$	$B_1 \oplus B_2$	$E$	2	0	-2	0	0

TABLE VII. Character tables of  $\mathbb{D}_{4d}$ ,  $\mathbb{C}_{4v}^b$ , and  $\mathbb{C}_{4v}^t$  point groups and their CRs.  $2\sigma_v^b/2\sigma_d^b$  and  $2\sigma_d^t/2\sigma_v^t$  respectively stand for the two classes  $\{\sigma_{v,i}^b\}$  and  $\{\sigma_{d,i}^b\}$  in  $\mathbb{C}_{4v}^b$  and the two classes  $\{\sigma_{d,i}^t\}$  and  $\{\sigma_{v,i}^t\}$  in  $\mathbb{C}_{4v}^t$ , with  $i = 0, 1$ .

$\mathbb{C}_{4v}^t$	$\mathbb{C}_{4v}^b$								
		$E$	$2C_4$	$C_2$	$2\sigma_d^t/2\sigma_v^t$	$E$	$2C_4$	$C_2$	$2\sigma_v^b/2\sigma_d^b$
	$\mathbb{D}_{4d}$	$E$	$2S_8$	$2C_4$	$2S_8^3$	$C_2$	$4C_2'$	$4\sigma_d$	
$A_1$	$A_1$	$A_1$	1	1	1	1	1	1	1
$A_2$	$A_2$	$A_2$	1	1	1	1	-1	-1	-1
$A_2$	$A_2$	$B_1$	1	-1	1	-1	1	1	-1
$A_1$	$A_1$	$B_2$	1	-1	1	-1	1	-1	1
$E$	$E$	$E_1$	2	$\sqrt{2}$	0	$-\sqrt{2}$	-2	0	0
$B_1 \oplus B_2$	$B_1 \oplus B_2$	$E_2$	2	0	-2	0	2	0	0
$E$	$E$	$E_3$	2	$-\sqrt{2}$	0	$\sqrt{2}$	-2	0	0

at  $\Gamma$  point for dodecagonal and octagonal vdW-QCs, as listed in Table VIII. Obviously the IHSRs for the first strongest resonant coupling in dodecagonal vdW-QC are the same as the IHSRs in real-space graphene quasicrystal due to the same symmetry restriction  $\mathbb{C}_{6v}^b + \mathbb{C}_{6v}^t \Rightarrow \mathbb{D}_{6d}$  [17].

We now numerically verify the IHSRs predicted by the CRs by virtue of the interlayer hybridization matrix element. Let us take  $\mathbb{D}_{nd}$  with  $n = 2, 4, 6$  at  $\Gamma$  point as an example. Eigenstates from each layer can be classified by the rotational operation  $C_n$ , i.e.,  $C_n|\varphi_{ir,\theta}^b\rangle = e^{i\theta}|\varphi_{ir,\theta}^b\rangle$  and  $C_n|\varphi_{ir',\theta'}^t\rangle = e^{i\theta'}|\varphi_{ir',\theta'}^t\rangle$ . Figure 6 shows the classified energy levels from each layer by  $C_n$  and the eigenenergy spectra of the first and second strongest resonant Hamiltonians. We can see that these hybridization-generated energy states are governed by Eqs. (21)–(26) in dodecagonal and octagonal vdW-QCs. We also figure out here that, in two middle subplots of Figs. 6(c) and 6(d),  $B_1$  and  $B_2$  states from the bottom and top  $\mathbb{C}_{4v}^{b/t}$  layers are directly converted into  $E_2$  bulk states of the coupled bilayers, because  $B_1$  and  $B_2$  states do not coexist in bottom

TABLE VIII. IHSRs and interlayer hybridization classifications in the first and second strongest resonant couplings of dodecagonal (dode) and octagonal (octa) vdW-QCs.

Systems	Order	Point groups	IHSRs	Interlayer hybridization classifications	
				Equivalent	Nonequivalent
dode	first	$\mathbb{D}_{6d}$	$U_{A_i,A_j} = \delta_{A_i,A_j} U_{A_i,A_j}$ $U_{E_i,E_j} = \delta_{E_i,E_j} U_{E_i,E_j}$ $U_{B_2,ir'} = \delta_{B_2,ir'} U_{B_2,ir'}$ $U_{B_1,ir'} = \delta_{B_2,ir'} U_{B_1,ir'}$	$A_1 + A_1 \Rightarrow A_1 + B_2$ $A_2 + A_2 \Rightarrow A_2 + B_1$ $E_1 + E_1 \Rightarrow E_1 + E_5$ $E_2 + E_2 \Rightarrow E_2 + E_4$	$B_1 + B_2 \Rightarrow E_3 + E_3$ $B_2 + B_1 \Rightarrow E_3 + E_3$
dode	second	$\mathbb{D}_{2d}$	$U_{A_i,A_j} = \delta_{A_i,A_j} U_{A_i,A_j}$ $U_{B_1,ir'} = \delta_{B_2,ir'} U_{B_1,ir'}$ $U_{B_2,ir'} = \delta_{B_1,ir'} U_{B_2,ir'}$	$A_1 + A_1 \Rightarrow A_1 + B_2$ $A_2 + A_2 \Rightarrow A_2 + B_1$	$B_1 + B_2 \Rightarrow E + E$ $B_2 + B_1 \Rightarrow E + E$
octa	first/second	$\mathbb{D}_{4d}$	$U_{A_i,A_j} = \delta_{A_i,A_j} U_{A_i,A_j}$ $U_{E,E} = \delta_{E,E} U_{E,E}$ $U_{B_1,ir'} = \delta_{B_2,ir'} U_{B_1,ir'}$ $U_{B_2,ir'} = \delta_{B_1,ir'} U_{B_2,ir'}$	$A_1 + A_1 \Rightarrow A_1 + B_2$ $A_2 + A_2 \Rightarrow A_2 + B_1$ $E + E \Rightarrow E_1 + E_3$	$B_1 + B_2 \Rightarrow E_2 + E_2$ $B_2 + B_1 \Rightarrow E_2 + E_2$
dode/octa	first/second	$\mathbb{C}_s$	$U_{A',A'} = \delta_{A',A'} U_{A',A'}$ $U_{A'',A''} = \delta_{A'',A''} U_{A'',A''}$	$A' + A' \Rightarrow A' + A'$ $A'' + A'' \Rightarrow A'' + A''$	
dode/octa	first/second	$\mathbb{C}_2$	$U_{A,A} = \delta_{A,A} U_{A,A}$	$A + A \Rightarrow A + B$	

TABLE IX. Character tables of  $\mathbb{C}_s$ ,  $\mathbb{C}_s^t$ , and  $\mathbb{C}_s^b$  point groups and their CRs.

$\mathbb{C}_s^t$	$\mathbb{C}_s^b$			
		$\mathbb{C}_s$	$E$	$\sigma_x$
			$E$	$\sigma_x$
$A'$	$A'$	$A'$	1	1
$A''$	$A''$	$A''$	1	-1

and top layers for the first two strongest resonant couplings in octagonal vdW-QC. In other words,  $B_1$  and  $B_2$  states from the bottom and top  $\mathbb{C}_{4v}^{b/t}$  layers are also the eigenstates of  $\mathbb{D}_{4d}$  bilayer system for the first two strongest resonant couplings in octagonal vdW-QC. In the basis functions of  $\mathbb{C}_6$ , the hybridization matrix elements satisfy  $U_{ir,ir'}^{\theta\theta'} = \delta_{\theta\theta'} U_{ir,ir'}^{\theta\theta'}$  [17]. Figure 7 shows  $|\langle \varphi_{ir,\theta}^t | U | \varphi_{ir',\theta'}^b \rangle|$  for the first and second strongest resonant couplings in dodecagonal and octagonal vdW-QCs. These nonzero matrix elements  $|\langle \varphi_{ir,\theta}^t | U | \varphi_{ir',\theta'}^b \rangle|$  manifest the IHSRs in Table VIII predicted by the CRs.

## B. IHSRs at $\mathbf{k}_0 \neq 0$ points

For  $\mathbf{k}_0$  shifting away from  $\Gamma$  point along  $-\mathbf{k}_x$  direction, these wave vectors  $\mathbf{Q}_i$  form the  $\mathbb{C}_s$  subspace with  $\mathbb{C}_s^b$  and  $\mathbb{C}_s^t$  symmetries for bottom and top layers for both the first and second strongest resonant couplings in dodecagonal and octagonal vdW-QCs [cf. Figs. 2(a) and 2(d), Figs. 3(a) and 3(d)]. Therefore, the interlayer hybridizations for  $\mathbf{k}_0$  in  $-\mathbf{k}_x$  direction follow the symmetry restriction  $\mathbb{C}_s^b + \mathbb{C}_s^t \Rightarrow \mathbb{C}_s$ . Using the character tables of  $\mathbb{C}_s$ ,  $\mathbb{C}_s^b$ , and  $\mathbb{C}_s^t$  point groups, we derive the CR between  $\mathbb{C}_s$  and  $\mathbb{C}_s^b$  and the CR between  $\mathbb{C}_s$  and  $\mathbb{C}_s^t$ , as listed in Table IX. We obtain the only allowed equivalent

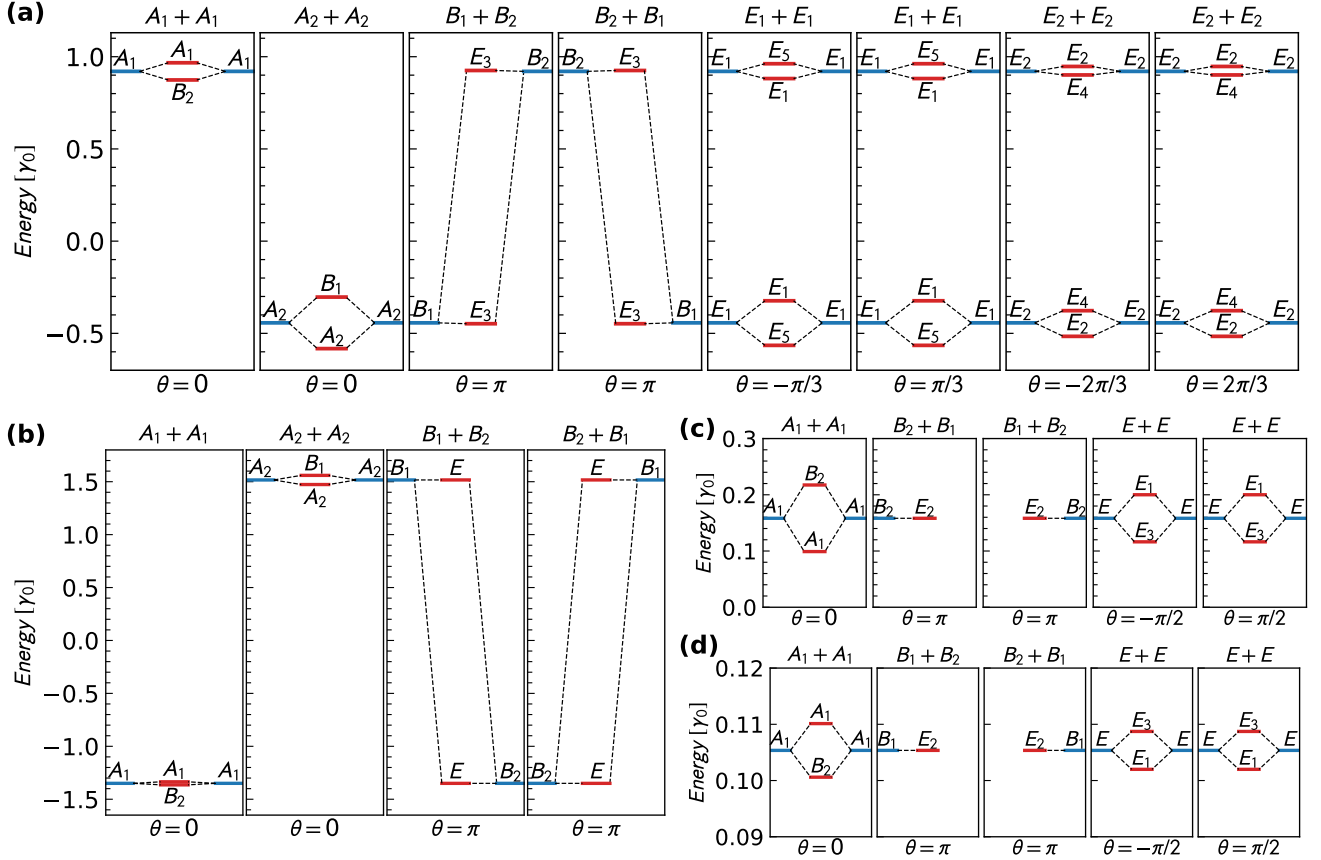


FIG. 6. (a) and (b) The classified eigenenergy spectra for the (first, second) strongest resonant coupling Hamiltonians at  $\Gamma$  point under  $(C_6, C_2)$  operations in dodecagonal vdW-QC. (c) and (d) The classified eigenenergy spectra for the (first, second) strongest resonant coupling Hamiltonians at  $\Gamma$  point under  $(C_4, C_4)$  operations in octagonal vdW-QC. In each subplot, the left and right blue lines stand for the energy levels of the bottom and top layers and the middle red lines for the coupled bilayer. The value of  $\theta$  corresponds to the eigenvalue  $e^{i\theta}$  of  $C_n$  acting on the eigenstates of the bottom and top layers.

hybridizations,

$$\begin{aligned} A' + A' &\Rightarrow A' + A', \\ A'' + A'' &\Rightarrow A'' + A''. \end{aligned} \quad (27)$$

For  $\mathbf{k}_0$  shifting away from  $\Gamma$  point along  $\Gamma \rightarrow O_0$  direction, these wave vectors  $\mathbf{Q}_i$  form the  $C_2$  subspace with  $C_1^b$  and  $C_1^t$  symmetries for bottom and top layers for both the first and second strongest resonant couplings in dodecagonal and octagonal vdW-QCs [cf. Figs. 2(c) and 2(f), Figs. 3(c) and 3(f)]. Therefore, the interlayer hybridizations for  $\mathbf{k}_0$  in  $\Gamma \rightarrow O_0$  direction follow the symmetry restriction  $C_1^b + C_1^t \Rightarrow C_2$ . Using the character tables of  $C_2$ ,  $C_1^b$ , and  $C_1^t$  point groups, we derive the CR between  $C_2$  and  $C_1^b$  and the CR between  $C_2$  and  $C_1^t$ , as listed in Table X. We obtain the only allowed equivalent hybridizations,

$$A + A \Rightarrow A + B. \quad (28)$$

Using Eqs. (27) and (28) we obtain the IHSRs at  $\mathbf{k}_0 \neq 0$  points for dodecagonal and octagonal vdW-QCs and also list them in Table VIII.

## VII. DISCUSSIONS

It is known that the dodecagonal vdW-QC has been realized experimentally[1,2] in the  $30^\circ$ -twisted bilayer graphene. The two-dimensional phthalocyanine-based metal-organic framework (MPC-MOF) [29] has an effective square lattice structure and energy bands contributed by the  $p_z$  orbitals of the carbon and nitrogen atoms around the Fermi energy. The  $45^\circ$ -twisted bilayer MPC-MOF is a candidate of the octagonal vdW-QC with eightfold rotational symmetry.

On the other hand, cold atom in optical lattices is a novel and powerful platform [19,20], which simulates various condensed-matter systems, such as the twisted bilayer

TABLE X. Character tables of  $C_2$ ,  $C_1^b$ , and  $C_1^t$  point groups and their CRs.

$C_1^t$	$C_1^b$	$C_2$		
		$E$	$E$	$C_{2,\Gamma O_0}$
$A$	$A$	$A$	1	1
$A$	$A$	$B$	1	-1

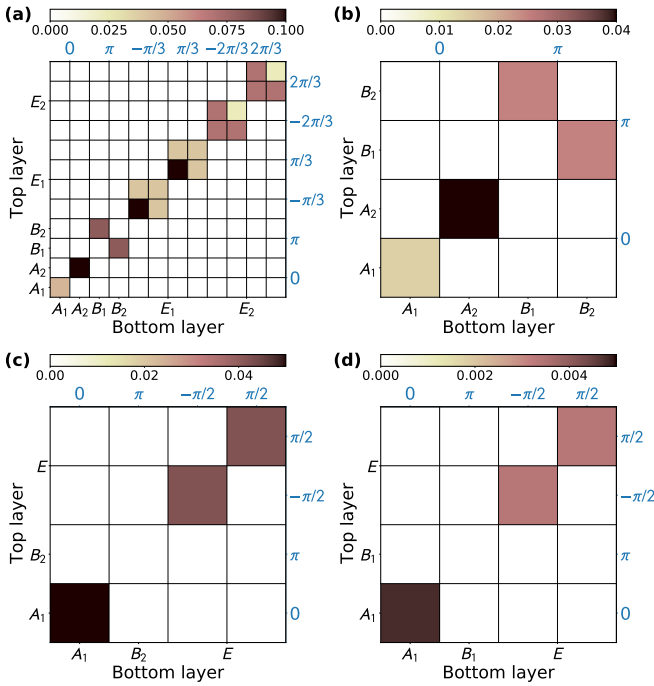


FIG. 7.  $|\langle \varphi_{ir,\theta}^b | U | \varphi_{ir',\theta'}^t \rangle|$  in unit of eV in (a) and (b) for the (first, second) strongest resonant couplings under  $(C_6, C_2)$  operations in dodecagonal vdW-QC.  $|\langle \varphi_{ir,\theta}^b | U | \varphi_{ir',\theta'}^t \rangle|$  in unit of eV in (c) and (d) for the (first, second) strongest resonant couplings under  $(C_4, C_4)$  operations in octagonal vdW-QC. The color map stands for the value of  $|\langle \varphi_{ir,\theta}^b | U | \varphi_{ir',\theta'}^t \rangle|$ , where  $|\varphi_{ir,\theta}^b\rangle$  and  $|\varphi_{ir',\theta'}^t\rangle$  are the eigenstates of the bottom and top layers. The value of  $\theta$  corresponds to the eigenvalue  $e^{i\theta}$  of  $C_n$  acting on the eigenstates of the bottom and top layers.

square optical lattice with controllable twist angle, intralayer hopping, and interlayer hopping [21,22]. In this respect, the  $45^\circ$ -twisted bilayer square lattice, i.e., the octagonal vdW-QC, can be realized experimentally in optical lattices.

In the twisted bilayer square optical lattice the Hamiltonian  $H$  is expanded in a separable Wannier basis  $w(\mathbf{r} - \mathbf{R}_{\alpha m})$ , where  $\mathbf{R}_{\alpha m}$  is the position of site  $m$  in layer  $\alpha$ . If the on-site interaction is tuned to a quite weak magnitude close to 0 through Feshbach resonances [30], the noninteracting Hamiltonian  $H$  reads [21]

$$H = H_{\text{intra}} + H_{\text{inter}}, \quad (29)$$

with

$$H_{\text{intra}} = - \sum_{m,n,\alpha} J_{\parallel}(\mathbf{R}_{\alpha m} - \mathbf{R}_{\alpha n}) a_{\alpha m}^\dagger a_{\alpha n}, \quad (30)$$

$$H_{\text{inter}} = \sum_{m,n,\alpha,\beta} J_{\perp}(\mathbf{R}_{\alpha m} - \mathbf{R}_{\beta n}) a_{\alpha m}^\dagger a_{\beta n},$$

where  $a_{\alpha m}^\dagger$  ( $a_{\beta n}$ ) is the creation (annihilation) operator for the Wannier function at  $\mathbf{R}_{\alpha,m}$  ( $\mathbf{R}_{\beta,n}$ ),  $J_{\parallel}(\mathbf{R}_{\alpha m} - \mathbf{R}_{\alpha n})$  is the intralayer hopping between the Wannier functions at site  $m$  and  $n$  of layer  $\alpha$ , and  $J_{\perp}(\mathbf{R}_{\alpha m} - \mathbf{R}_{\beta n})$  is the interlayer hopping between the Wannier functions at site  $m$  of layer  $\alpha$  and at site  $n$  of layer  $\beta$ .  $J_{\parallel}(\mathbf{R}_{\alpha m} - \mathbf{R}_{\alpha n})$  and  $J_{\perp}(\mathbf{R}_{\alpha m} - \mathbf{R}_{\beta n})$  have the

following expressions [21,30]:

$$J_{\parallel}(\mathbf{R}_{\alpha m} - \mathbf{R}_{\alpha n}) \propto E_R e^{-\frac{1}{4L_0^2}(\mathbf{R}_{\alpha m} - \mathbf{R}_{\alpha n})^2},$$

$$J_{\perp}(\mathbf{R}_{\alpha m} - \mathbf{R}_{\beta n}) \propto \Omega_{\perp} e^{-\frac{1}{4L_0^2}(\mathbf{R}_{\alpha m} - \mathbf{R}_{\beta n})^2}. \quad (31)$$

Here  $E_R = \frac{\hbar^2 k^2}{2M}$  is the recoil energy with the atom mass  $M$  and  $k = \frac{2\pi}{\lambda}$  with  $\lambda$  being the wavelength of the laser,  $\Omega_{\perp}$  controls the strength of the interlayer coupling and can be tuned independently through a direct microwave transition or a two-photon Raman process, and  $L_0 = \sqrt{\frac{\hbar}{M\omega_t}}$  is the size of ground-state wave function with  $\omega_t$  being the trapping frequency. As a result of the same symmetry of the twisted bilayer square lattice and only one orbital in each site, Eqs. (31) and (6) have very similar expressions. We can obtain the transformation between hopping parameters for the octagonal vdW-QC from Eq. (31) to Eqs. (4) and (6). At last, we emphasize that our symmetry analyses, compatibility relationships, band splits, and IHSRs are a result of lattice symmetry and hence they are independent of numerical values of these tight-binding parameters.

## VIII. CONCLUSION

We investigated the symmetries of both the first and second strongest resonant coupling Hamiltonians, which endow the quasiband structures describing electronic properties of dodecagonal and octagonal vdW-QCs. Our symmetry analyses indicate that (i) the Hamiltonian has the highest  $\mathbb{D}_{nd}$  symmetries at  $\Gamma$  point for the first ( $n = 6$ ) and second ( $n = 2$ ) strongest resonant couplings in dodecagonal vdW-QC and for both first two strongest resonant couplings in octagonal vdW-QC with  $n = 4$ , and (ii) the Hamiltonian has respectively  $C_s$  and  $C_2$  symmetries for  $-\mathbf{k}_x$  and  $\Gamma \rightarrow O_0$  pathways in both dodecagonal and octagonal vdW-QCs. The derived CRs predict that in the quasiband structures the degenerate  $E_i$  (or  $E$ ) states at  $\Gamma$  point are split into one  $A'$  and one  $A''$  state along  $-\mathbf{k}_x$  direction and into one  $A$  and one  $B$  state along  $\Gamma \rightarrow O_0$  direction due to the decreasing symmetries. We use the CRs of different point groups between the coupled bilayers and uncoupled monolayers to derive the IHSRs of both the first two strongest resonant couplings in dodecagonal and octagonal vdW-QCs. Our results show that the resonant couplings allow nonequivalent hybridizations only between  $B_1$  and  $B_2$  states and equivalent hybridizations for  $A, A_i, A', A'', E$ , or  $E_i$  states. Numerical results of the energy spectra and nonzero interlayer hybridization matrix element distributions further verify these IHSRs predicted by the CRs.

## ACKNOWLEDGMENTS

S.Y. acknowledges support from the National Science Foundation of China (No. 12174291). H.-Q.L. and Y.W. acknowledge financial support from NSAF (No. U1930402), NSFC (No. 11734002 and No. 12088101) and computational resources from the Beijing Computational Science Research Center. G.Y. and Y.W. acknowledge support from the China Postdoctoral Science Foundation (Grants No. 2018M632902 and No. 2019M660433) and NSFC (No. 11832019). M.I.K. acknowledges support from the ERC Synergy Grant, Project No. 854843 FASTCORR.

- [1] S. J. Ahn, P. Moon, T.-H. Kim, H.-W. Kim, H.-C. Shin, E. H. Kim, H. W. Cha, S.-J. Kahng, P. Kim, M. Koshino, Y.-W. Son, C.-W. Yang, and J. R. Ahn, *Science* **361**, 782 (2018).
- [2] W. Yao, E. Wang, C. Bao, Y. Zhang, K. Zhang, K. Bao, C. K. Chan, C. Chen, J. Avila, M. C. Asensio, J. Zhu, and S. Zhou, *Proc. Natl. Acad. Sci.* **115**, 6928 (2018).
- [3] C. Yan, D.-L. Ma, J.-B. Qiao, H.-Y. Zhong, L. Yang, S.-Y. Li, Z.-Q. Fu, Y. Zhang, and L. He, *2D Mater.* **6**, 045041 (2019).
- [4] T. Suzuki, T. Iimori, S. J. Ahn, Y. Zhao, M. Watanabe, J. Xu, M. Fujisawa, T. Kanai, N. Ishii, J. Itatani, K. Suwa, H. Fukidome, S. Tanaka, J. R. Ahn, K. Okazaki, S. Shin, F. Komori, and I. Matsuda, *ACS Nano* **13**, 11981 (2019).
- [5] F. C. Bocquet, Y.-R. Lin, M. Franke, N. Samiresht, S. Parhizkar, S. Soubatch, T.-L. Lee, C. Kumpf, and F. S. Tautz, *Phys. Rev. Lett.* **125**, 106102 (2020).
- [6] J. Liu, Z. Wang, D. Ling, D. Wei, W. Lv, X. Kang, F. Qi, S. Ding, X. Hao, P. Li, and Y. Chen, *2D Mater.* **8**, 021002 (2021).
- [7] S. Pezzini, V. Mišeikis, G. Piccinini, S. Forti, S. Pace, R. Engelke, F. Rossella, K. Watanabe, T. Taniguchi, P. Kim, and C. Coletti, *Nano Lett.* **20**, 3313 (2020).
- [8] Y. Takesaki, K. Kawahara, H. Hibino, S. Okada, M. Tsuji, and H. Ago, *Chem. Mater.* **28**, 4583 (2016).
- [9] Y. Fukaya, Y. Zhao, H.-W. Kim, J. R. Ahn, H. Fukidome, and I. Matsuda, *Phys. Rev. B* **104**, L180202 (2021).
- [10] G. Yu, M. I. Katsnelson, and S. Yuan, *Phys. Rev. B* **102**, 045113 (2020).
- [11] J. A. Crosse and P. Moon, *Phys. Rev. B* **103**, 045408 (2021).
- [12] S. Spurrier and N. R. Cooper, *Phys. Rev. B* **100**, 081405(R) (2019).
- [13] E. Koren and U. Duerig, *Phys. Rev. B* **93**, 201404(R) (2016).
- [14] D. Shechtman, I. Blech, D. Gratias, and J. W. Cahn, *Phys. Rev. Lett.* **53**, 1951 (1984).
- [15] D. Levine and P. J. Steinhardt, *Phys. Rev. Lett.* **53**, 2477 (1984).
- [16] P. Moon, M. Koshino, and Y.-W. Son, *Phys. Rev. B* **99**, 165430 (2019).
- [17] G. Yu, Y. Wang, M. I. Katsnelson, H.-Q. Lin, and S. Yuan, *Phys. Rev. B* **105**, 125403 (2022).
- [18] J. C. Slater and G. F. Koster, *Phys. Rev.* **94**, 1498 (1954).
- [19] I. Bloch, J. Dalibard, and S. Nascimbène, *Nat. Phys.* **8**, 267 (2012).
- [20] M. Lewenstein, A. Sanpera, V. Ahufinger, B. Damski, A. Sen(De), and U. Sen, *Adv. Phys.* **56**, 243 (2007).
- [21] A. González-Tudela and J. I. Cirac, *Phys. Rev. A* **100**, 053604 (2019).
- [22] Z. Meng, L. Wang, W. Han, F. Liu, K. Wen, C. Gao, P. Wang, C. Chin, and J. Zhang, *arXiv:2110.00149*.
- [23] G. Yu, Z. Wu, Z. Zhan, M. I. Katsnelson, and S. Yuan, *Phys. Rev. B* **102**, 115123 (2020).
- [24] M. Koshino, *New J. Phys.* **17**, 015014 (2015).
- [25] R. Bistritzer and A. H. MacDonald, *Proc. Natl. Acad. Sci. USA* **108**, 12233 (2011).
- [26] S. Shallcross, S. Sharma, E. Kandelaki, and O. A. Pankratov, *Phys. Rev. B* **81**, 165105 (2010).
- [27] S. Shallcross, S. Sharma, and O. Pankratov, *Phys. Rev. B* **87**, 245403 (2013).
- [28] D. Weckbecker, S. Shallcross, M. Fleischmann, N. Ray, S. Sharma, and O. Pankratov, *Phys. Rev. B* **93**, 035452 (2016).
- [29] W. Jiang, S. Zhang, Z. Wang, F. Liu, and T. Low, *Nano Lett.* **20**, 1959 (2020).
- [30] I. Bloch, J. Dalibard, and W. Zwerger, *Rev. Mod. Phys.* **80**, 885 (2008).